Differential sensitivity to hypoxia enables shape-based classification of sickle cell disease and trait blood samples

Claudy D'Costa[a,1], Oshin Sharma[a,1], Riddha Manna[a], Minakshi Singh[a], Samrat[a,b], Srushti Singh[a,b], Anish Mahto[a], Pratiksha Govil[a], Sampath Satti[a], Ninad Mehendale[a], and Debjani Paul[a,c,2]

[a]Department of Biosciences and Bioengineering, Indian Institute of Technology Bombay, Powai, Mumbai 400076, Maharashtra, India

[b]MedPrime Technologies Pvt. Ltd., Casa Piedade Co-operative Housing Society, Charai, Thane – 400601, Maharashtra, India

[c]Associate faculty, Wadhwani Research Centre for Bioengineering, Indian Institute of Technology Bombay, Powai, Mumbai 400076, Maharashtra, India

[1]Equal contributions

[2]To whom correspondence may be addressed: debjani.paul@iitb.ac.in; ORCID: 0000-0001-9281-3516

Keywords: sickle cell anemia diagnosis, smartphone microscopy, microfluidics, RBC shapes, shape-based classifier

Abstract

In sickle cell anemia patients, red blood cells (RBCs) are known to become sickle shaped and stiff under hypoxic conditions as a consequence of hemoglobin polymerization. While RBC shape can discriminate sickle blood from healthy, it has not been used until now as a sole biophysical marker to differentiate between homozygous (disease) and heterozygous (trait) sickle blood samples. Here, we establish a technique based on the differential response of disease and trait RBCs to chemically-induced hypoxia to distinguish between these samples for the first time. By comparing the RBC shape distributions in blood treated with high and low concentrations of the hypoxia-inducing agent, we correctly identify 35 unknown blood samples as healthy, sickle cell disease or trait. Finally, we demonstrate our image-based classification technique with a portable smartphone microscope and a disposable microfluidic chip as a prospective point-of-care device enabling fast and confirmed diagnosis of sickle cell anemia.

Significance statement

Red blood cells (RBCs) of individuals with sickle cell anemia exhibit characteristic shapes in low oxygen environments. The shape of a sickle RBC is determined by its hemoglobin content and how fast oxygen is removed from its surroundings. We report a technique to distinguish between sickle cell carriers and individuals with sickle cell anemia within an hour by treating whole blood with a chemical that removes oxygen, imaging the blood sample inside a microfluidic chamber using a smartphone microscope and finally comparing the shapes of the sickle cells using a classification scheme. We demonstrate the proof of concept of a biophysical test based on the analysis of RBC shapes for point-of-care diagnosis of sickle cell disease in low resource settings.

Main

Sickle cell anemia is a genetic disorder caused by a glutamine to valine mutation in the β-globin gene [1]. It results in partial or complete replacement of normal adult hemoglobin (HbA) with mutated sickle hemoglobin (HbS). HbS polymerizes under hypoxic conditions and forms rigid and misshapen red blood cells (RBCs). The loss of deformability of RBCs leads to frequent vaso-occlusive crisis, joint pain, spleen damage, increased susceptibility to infection and anemia. While there is no cure available for sickle cell anemia, early diagnosis can prevent child mortality and improve the quality of life of the affected individuals.

The disease is prevalent in many parts of the world including western Africa, Latin America, the Arab peninsula, and India [2]. More than 500 children die of sickle cell anemia every day due to lack of diagnosis [3]. There are no comprehensive pre-natal and newborn screening programs in low- and medium-income countries (LMIC). Screening and diagnosis of older adults in LMICs are carried out in two stages. First, a solubility test screens for HbS-positive individuals. Second, hemoglobin electrophoresis or high-performance liquid chromatography (HPLC) confirms the diagnosis and distinguishes sickle cell disease (homozygous) from trait (heterozygous) [4]. The infrastructure and the trained personnel required to perform these tests are not always available in LMICs to sustain countrywide screening programs [5].

Preparation of blood smear slides and their microscopic examination are diagnostic techniques that are relatively easier to administer in LMICs. Despite the widespread use of microscopy to study sickle blood in the early days [6] [7] [8] [9], it is no longer a technique preferred by the clinicians. Sickle blood has only 5% - 25% irreversibly sickled cells (ISCs) [10], requiring extensive scanning of each smear slide by a technician. While use of a chemical oxygen scavenger, such as sodium dithionate or sodium metabisulphite, allows more RBCs to sickle *in vitro*, the process can take as long as 24 hours for trait blood samples. Most importantly, it is not possible to conclusively distinguish between sickle cell disease and trait blood by simple visual inspection of RBC shapes.

Several research groups have explored image processing or machine learning techniques to study RBC morphologies [11] [12] [13] [14] [15] [16] [17] [18]. These techniques have focused on accurate classification of individual RBC shapes into normal (biconcave), sickle or abnormal (i.e. having any shape other than biconcave or sickle). None of these reports have used RBC shape as a sole biophysical marker to classify sickle blood samples into disease or trait. Recently, Javidi and others classified blood samples into healthy and sickle based on membrane fluctuation analysis of individual RBCs [19]. De Haan *et al* developed a mobile phone microscope to image blood smears, followed by automated identification of ISCs in these images [20]. As a shortcoming of their method, the authors stated that blood smears cannot be used to identify sickle cell genotypes, i.e. to discriminate between trait and disease blood samples.

Here, we combine microfluidics, smartphone microscopy and image processing techniques (**figure 1**) to develop a method that accurately distinguishes between disease and trait sickle blood based on the differential shape changes of RBCs when treated with two different concentrations of an oxygen scavenger, sodium metabisulphite. As shown in **figure 1A**, the method consists of mixing a drop of blood with a specific concentration of sodium metabisulphite, loading it into a

microfluidic chip and imaging the sickled RBCs in real time using a smartphone microscope. The roundness distributions of RBCs after 30 min are used to classify the blood sample as healthy, disease or trait. The use of a microfluidic chip (**figure 2B**) as an imaging chamber instead of a smear slide enables fast sickling and

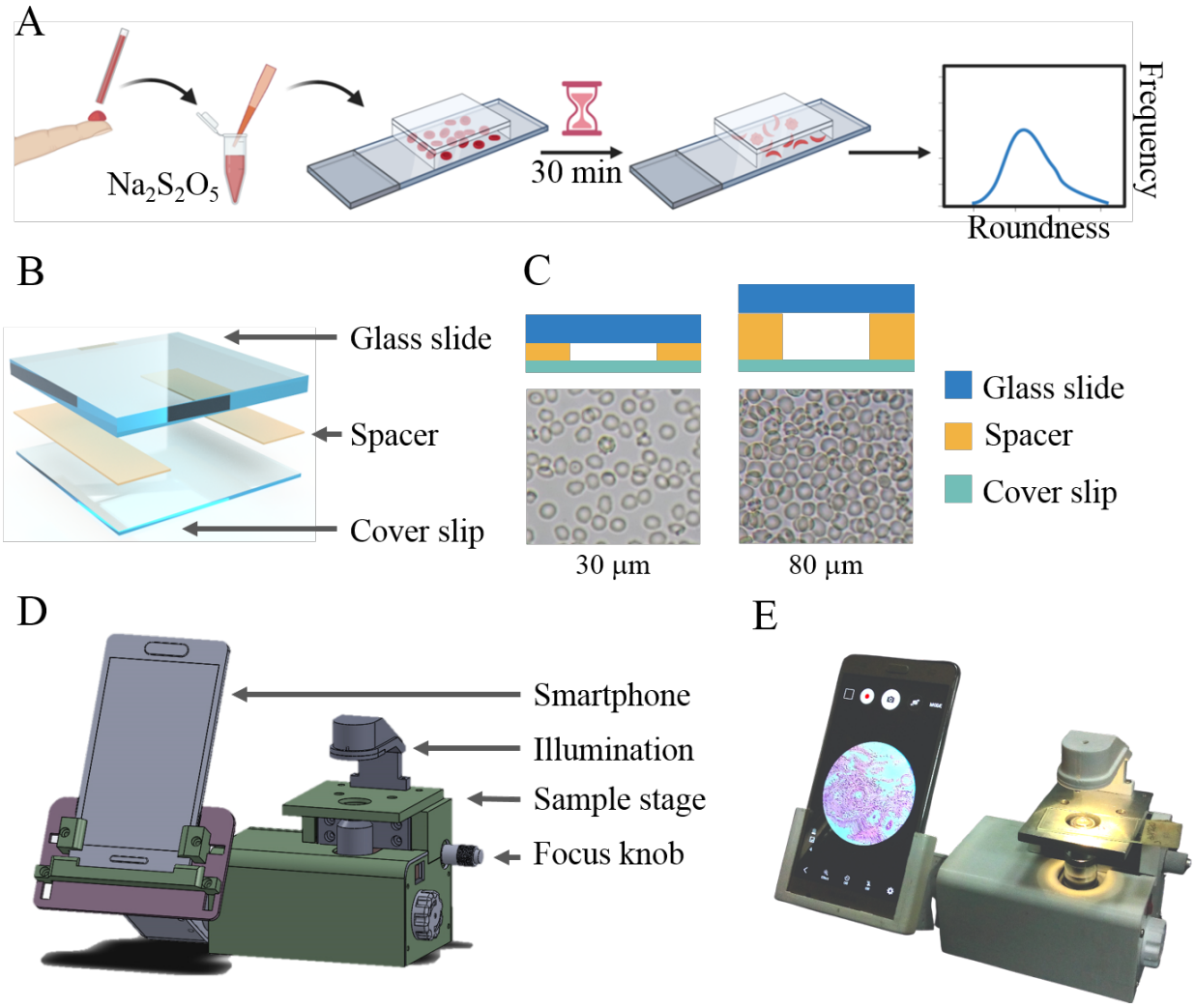

Figure 1. An assay to induce controlled sickling of RBCs inside a microfluidic chip, followed by imaging and analysis of RBC shapes. (A) A drop of blood is added to an oxygen scavenger ($Na_2S_2O_5$), introduced into a microfluidic chamber and sealed. We image the sample after 30 min and analyze the RBC shapes to obtain a characteristic roundness distribution. (B) Exploded view of the microfluidic chamber. The thickness of the spacer determines the height of the chamber. (C) Optimisation of microfluidic chamber height. RBCs inside a 30 µm high chamber are oriented flat, while they are stacked and randomly oriented when the height is 80 µm. (D) Schematic diagram of the microscope showing LED illumination, sample stage and the focusing knob. (E) A photo of the portable smartphone microscope designed and fabricated by us.

tracking of RBC shapes in real time. The chip is made of glass to facilitate brightfield imaging of unstained RBCs using a mobile phone microscope and to maintain hypoxic conditions inside the chamber for the duration of the experiment. We optimized the height of the chamber to be 30 μm (**figure 1C**) to avoid stacking of RBCs. We also designed and fabricated a portable smartphone microscope (**figures 1D** and **1E**) to conduct our experiments outside the laboratory at sickle cell screening camps. More details about optimizing the microfluidic chip design (**figure S1**) and the smartphone microscope (**figure S2**) can be found in the supporting information.

Difference in polymerization of sickle hemoglobin in disease and trait blood leads to different RBC shapes

I. J. Sherman first connected the shapes of sickled RBCs to the rate of oxygen removal by noting that slow deoxygenation resulted in RBCs with sickle shapes, while sudden deoxygenation made them granular. He reported that disease blood had more sickled RBCs in it compared to trait blood [6]. A relation between RBC shapes and polymerization kinetics of sickle hemoglobin (HbS) was later proposed by Eaton and Hofrichter. Based on extensive *in vitro* studies on HbS, they predicted that sickle shapes of RBCs are likely to result from the growth of a single polymer domain during slow polymerization. Presence of multiple small polymer domains with shorter fibers should lead to holly leaf cell shapes. When there are many more randomly oriented and very short fibers, RBCs will become granular [21]. Direct experimental evidence of this prediction using linear dichroism microscopy was provided by Mickols et al [22] and by Corbett et al [23]. They measured the distribution and orientation of aligned hemoglobin polymer domains inside RBCs and related it to different cell shapes.

Figure 2 illustrates different HbS polymerization mechanisms in disease and trait blood and the associated RBC shapes. The total hemoglobin in homozygous sickle blood consists of 95% - 98% HbS, 2% - 3% HbA_2 (another variant of normal hemoglobin) and 2% HbF (fetal hemoglobin). Heterozygous sickle cell blood contains 35% - 45% HbS, 50% - 65% HbA, 2% - 3% HbA_2 and ~ 2% HbF [24]. As shown in **figure 2A**, blood from healthy individuals has HbAA homodimers ($\alpha_2\beta_2$), sickle cell disease blood has HbSS homodimers ($\alpha_2\beta^S{}_2$), and trait blood contains a mix of HbAA homodimers ($\alpha_2\beta_2$), HbSS homodimers ($\alpha_2\beta^S{}_2$) and HbAS heterodimers ($\alpha_2\ \beta\beta^S$).

According to the double nucleation model proposed by Ferrone *et al*, hemoglobin polymerization can proceed by homogenous or heterogeneous nucleation (**figure 2B**) [25]. Homogeneous nucleation involves growth of independent polymer chains from HbS molecules in solution, whereas heterogeneous nucleation involves formation of branches on already existing polymers. Even though homogeneous nucleation is thermodynamically less favorable, Ferrone and others suggested that it can be sustained in samples with high initial HbS concentration for a longer duration before heterogeneous nucleation takes over. Since sickle cell disease blood has high HbS concentration, we infer that these samples are likely to sustain homogeneous nucleation for some time. The authors further observed that fast deoxygenation leads to more homogeneous nucleation sites and formation of randomly oriented polymer chains. Hence, we expect that faster

deoxygenation in disease samples would lead to more granular RBCs and very few, if any, sickle-shaped RBCs. Slow deoxygenation in these samples would lead to sickle RBCs, resulting from sustained homogeneous nucleation, as well as some holly leaf and granular RBCs formed due to heterogeneous nucleation.

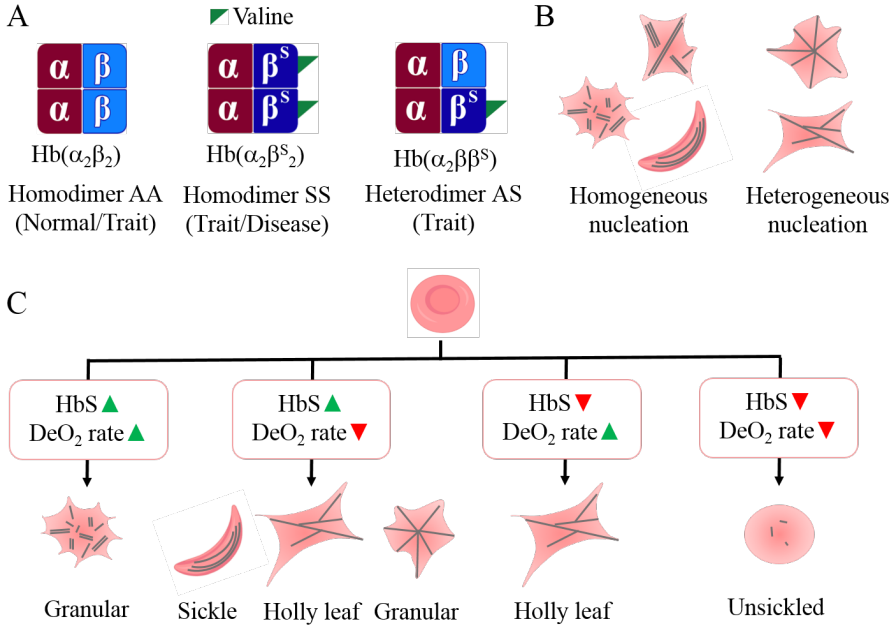

Figure 2. Schematic diagram relating hemoglobin polymerization to the shapes of sickled RBCs. (A) Hemoglobin in healthy blood samples exists as homodimer A ($\alpha_2\beta_2$). This homodimer is also found in trait blood. Sickle hemoglobin can either exist as a homodimer S ($\alpha_2\beta^S{}_2$) found in both trait and disease blood, or as a heterodimer ($\alpha_2\beta\beta^S$), found only in trait blood. (B) During hemoglobin polymerization, homogeneous nucleation leads to one or more non-branched polymer chains, while heterogeneous nucleation leads to branched polymers. The type of hemoglobin polymerization taking place inside an RBC affects its shape. (C) A pictorial summary of how shapes of sickled RBCs depend on HbS concentration and deoxygenation rate. Green 'up triangle' symbol indicates a high HbS concentration or fast deoxygenation. Red 'down triangle' symbol indicates low HbS concentration or slow deoxygenation.

In addition to HbS concentration and the rate of deoxygenation, HbS polymerization in trait samples is also affected by the presence of HbAS heterodimers which can constitute as much as ~ 49% mole fraction of the total hemoglobin [26]. HbS concentration in trait samples is too low to sustain homogeneous nucleation. Moreover, HbAS heterodimers have a lower probability to take part in polymerization compared to HbSS homodimers [27]. Under slow deoxygenation, due to a lack of nucleation sites, RBC morphology in trait blood appears to be unchanged. When deoxygenation is rapid, trait RBCs deform into primarily holly leaf shapes resulting from heterogeneous nucleation. **Figure 2C** summarizes the combined effect of HbS concentration and rate of deoxygenation on RBC shapes. Our shape-based classification method to identify unknown

blood samples makes use of the variation in RBC shapes in disease and trait samples in response to slow and fast deoxygenation.

Specific concentrations of sodium metabisulphite lead to slow and fast deoxygenation

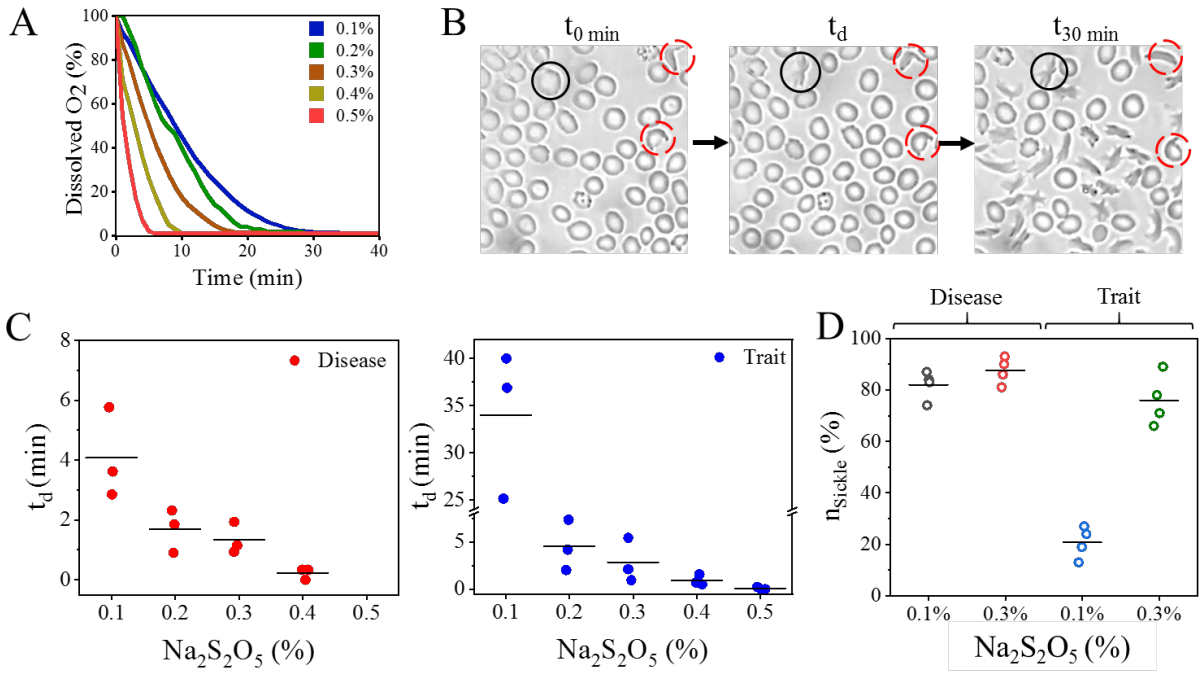

Figure 3. Optimization of sodium metabisulphite concentration to induce slow and fast deoxygenation in disease and trait blood samples. (A) Decrease in the dissolved oxygen in cell culture media (RPMI-1640) with time for different concentrations of sodium metabisulphite. (B) Schematic representation of the time (t_d) taken by the first unsickled RBC (enclosed by the black circle) in the field of view to sickle. Irreversibly sickled RBCs are encircled in dashed red. (C) t_d as a function of sodium metabisulphite concentration in three distinct disease and three distinct trait samples, represented as mean ± SEM (N = 3). (D) Number of sickled RBCs in disease (N = 4) and trait (N = 4) samples treated with 0.1% and 0.3% sodium metabisulphite respectively. The horizontal lines indicate the mean values in all the plots in (C) and (D).

We optimized the concentration (w/v) of sodium metabisulphite with the goal of identifying two specific concentrations at which disease and trait samples are likely to undergo slow and fast deoxygenation resulting in different RBC shapes. We added 0.1% to 0.5% of sodium metabisulphite to cell culture media (RPMI-1640) and measured its dissolved oxygen content for 40 min. **Figure 3A** shows a plot of the dissolved oxygen content as a function of time for different concentrations of sodium metabisulphite. For the entire range of concentrations studied, the oxygen content of RPMI-1640 decreased to <5% within 30 min, which is considered to be the physiological level of deoxygenation in blood [28].

We then prepared 0.1% to 0.5% sodium metabisulphite solutions in cell culture media and mixed with disease and trait blood samples such that blood is diluted by $20X$ after mixing (**table S1** and **figure S3** in supporting information). We recorded real time sickling videos in our smartphone microscope, and from the extracted frames, determined the instant (t_d) at which the first unsickled RBC in the field of view starts sickling. **Figure 3B** shows how t_d is measured for the RBC indicated by the solid black circle, with the first frame in the video taken as the timepoint $t = 0$ min. RBCs inside the dashed red circles are already sickled, and therefore, are not considered for this purpose.

We then used t_d as a parameter to compare the sickling behavior of disease and trait RBCs treated with different sodium metabisulphite concentrations. **Figure 3C** shows how t_d varies with sodium metabisulphite concentration for three disease and three trait samples. For disease samples treated with 0.1%, 0.2% and 0.3% concentrations, t_d is 4.1 min ± 0.9 min (mean ± SEM), 1.7 ± 0.4 min and 1.3 ± 0.3 min respectively. The corresponding values for trait samples are 33.4 ± 4.8 min, 4.5 ± 1.5 min and 2.8 ± 1.3 min respectively. Since sickling occurs almost instantaneously at 0.4% and 0.5% concentrations, making it difficult to accurately measure t_d, these two concentrations were not considered further.

While 82 ±3 % (mean ± SEM) of RBCs in disease blood sickle within 30 min when treated with 0.1 % concentration, only 21 ± 3% of RBCs in trait blood sickle at this concentration (**figure 3D**). In contrast, the average number of sickled RBCs in disease and trait blood samples treated with 0.3% sodium metabisulphite for 30 min are 88 ± 3 % and 76 ± 5% respectively.

Therefore, based on the differential sickling response of RBCs in our experiments, we chose 0.1% and 0.3% as the two sodium metabisulphite concentrations to induce slow and fast deoxygenation respectively in sickle blood samples. The experiments on quantifying the shape distribution of RBCs were performed with these two sodium metabisulphite concentrations.

Deoxygenated healthy, disease and trait blood have characteristic roundness distributions

We treated three samples each of healthy, disease and trait blood with 0.1% and 0.3% sodium metabisulphite and imaged the RBCs after 30 min. Images of RBCs in the same samples, without oxygen scavenger, were also captured as negative controls. **Figure 4A** shows snippets of representative images from healthy, disease and trait blood samples, where the individual RBCs exhibit a range of shapes (**figure 4B**). The complete raw images from which the snippets are taken are shown in **figure S4** in the supporting information.

Wheeless et al reported form factor (FF), given by equation (1), to be the most suitable image analysis feature to distinguish between sickle RBC shapes after comparing 42 shape descriptors [12]. As shown in **figure S5** in the supporting information, we found roundness (R), given by equation (2), to be a more accurate measure of RBC shapes in our images when compared to the form factor.

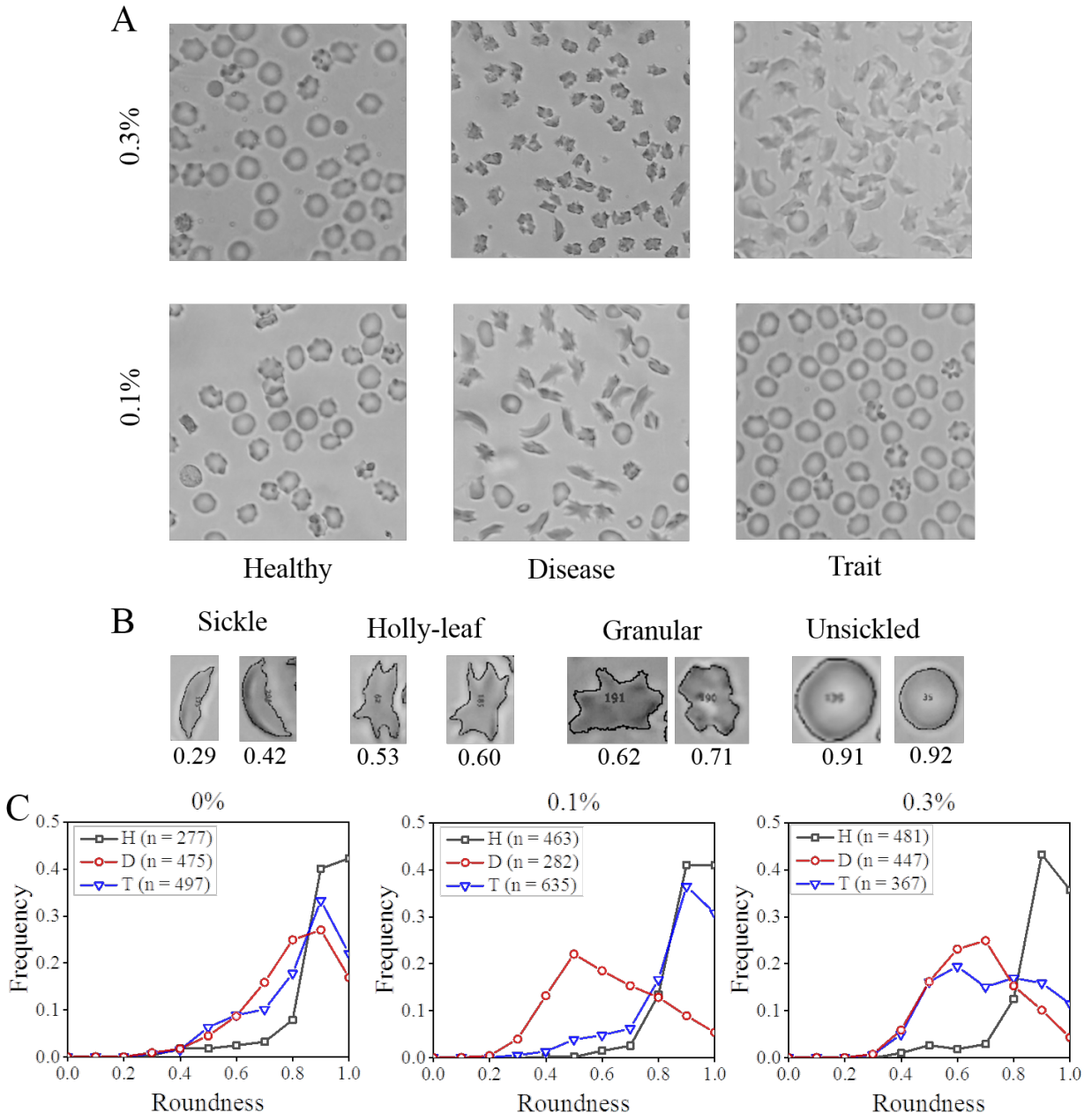

Figure 4. Roundness as a shape descriptor for quantifying RBC shapes in healthy and sickle blood. (A) Snippets of representative images of healthy, disease and trait samples treated with 0.1% and 0.3% sodium metabisulphite for 30 min are shown. Some crenated RBCs are seen in both the healthy samples and the trait blood sample treated with 0.1% sodium metabisulphite. (B) Sickle RBCs under hypoxia have a range of shapes which can be characterized by a roundness value. (C) Roundness distributions of RBCs in healthy (H; black square), disease (D; red circle) and trait (T; blue triangle) samples treated with 0%, 0.1% and 0.3% sodium metabisulphite respectively are shown. Each distribution is generated by analysing three different blood samples (N =3) and then pooling the data to see the overall trend. Here, n indicates the total number of RBCs in three samples used to generate each roundness distribution plot. Each plot is normalized by dividing it by the number of RBCs (n).

$$FF = \frac{4 \times \pi \times Area}{Perimeter^2} \quad (1)$$

$$R = \frac{4 \times Area}{\pi \times Major\ axix^2} \quad (2)$$

Figure 4C shows the roundness distribution plots of RBCs in healthy (indicated by black square), disease (red circle) and trait (blue triangle) blood, where each curve has data pooled from three samples and n indicates the number of RBCs from these three samples used to generate each distribution plot. The left panel shows the control distributions in absence of the oxygen scavenger. The distribution corresponding healthy blood peaks at 1.0 as healthy biconcave RBCs lying flat inside the imaging chamber appear circular in shape. The distributions for trait and disease samples peak at 0.9 due to the presence of very few ISCs. The disease distribution has a broader peak compared to the trait distribution as disease samples have more ISCs than trait samples.

The middle panel shows the roundness distributions of blood samples treated with 0.1% sodium metabisulphite. Healthy RBCs show a peak at 0.9 – 1.0 as these do not sickle when treated with an oxygen scavenger. Due to a combination of slower deoxygenation and high HbS concentration, RBCs in disease samples have a mix of sickle, holly leaf and granular shapes (also see **figure 2C and figures S6** and **S7** in supporting information), resulting in a broad distribution with a peak at 0.5. As the shapes of most RBCs in trait blood samples treated with 0.1% sodium metabisulphite remain unchanged owing to fewer nucleation sites, presence of HbAS heterodimers, and slow deoxygenation, the resulting roundness distribution peaks at 0.9, similar to healthy RBCs.

The right panel shows roundness distributions resulting from treatment with 0.3% sodium metabisulphite. A combination of faster deoxygenation and higher HbS concentration in disease samples results in granular RBCs, which is reflected in a broad distribution with a peak at 0.7. On the other hand, owing to faster deoxygenation and lower HbS concentration, RBCs assume holly leaf shapes in trait samples. This leads to a somewhat bimodal roundness distribution with peaks at 0.6 and 0.8 respectively. As expected, the distribution for healthy RBCs has a peak at 0.9. The tails of the distributions for healthy RBCs at lower roundness values in all three panels result from certain analysis artifacts, as shown in **figure S8** in the supporting information.

As RBCs with holly leaf and granular shapes have similar roundness, the roundness distributions of trait and disease samples treated with 0.3% sodium metabisulphite overlap with each other. Similarly, the peaks for distributions corresponding to healthy and trait samples treated with 0.1% sodium metabisulphite overlap. Therefore, the position of the peaks alone is not sufficient distinguish between these samples.

A shape-based classifier distinguishes between healthy and sickle blood

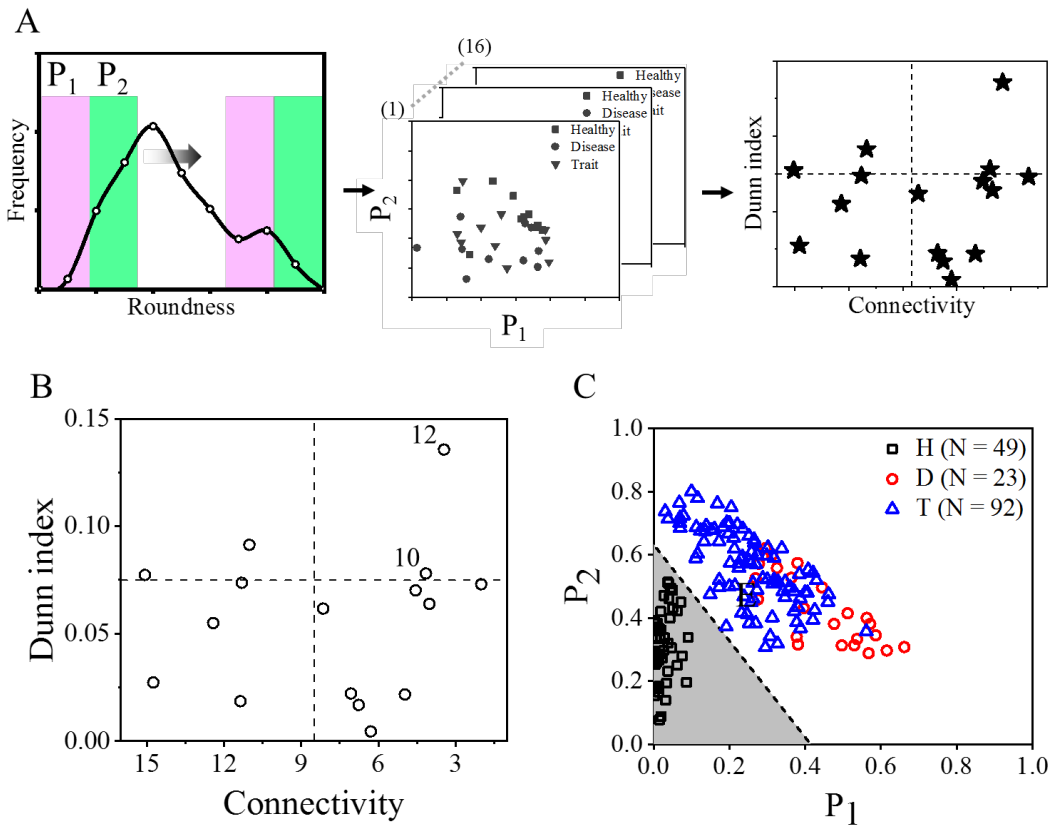

Figure 5. Derivation of two secondary shape parameters P_1 and P_2 from the roundness distributions. (A) Schematic diagram describing the process flow to choose a robust combination of P_1 and P_2. (B) A plot of Dunn index vs connectivity for 16 unique combinations of P_1 and P_2 corresponding to 164 blood samples. The top-right quadrant of the plot indicates the most robust combinations (e.g. 10 and 12) with low connectivity and high Dunn index values. (C) Development of the classifier. P_2 vs P_1 data for 164 distinct blood samples with known haemoglobin profiles are plotted. Two distinct clusters are seen, one for the normal samples (HbA), and one for the trait and diseased samples (HbS). The classifier (dotted line) separates the parameter space into two regions indicated in grey and white.

We derived two secondary shape parameters P_1 and P_2 from each roundness distribution, using a process flow shown schematically in **figure 5A**. We identified two specific areas under each roundness distribution curve by placing two contiguous windows of equal width (left panel). We called these two areas parameter 1 (P_1; violet) and parameter 2 (P_2; green) respectively. Each roundness distribution is represented as a single point on a plot of P_2 vs. P_1. We then translated the pair of windows by increments of 0.1 over the entire range of roundness values, while also varying their widths from 0.2 to 0.5, and calculated all sixteen P_1 - P_2 combinations resulting from this operation (middle panel). Widths <0.2 were not considered as they would contain information about very few RBCs. We then ran a k-means algorithm on each of these 16 datasets to distinguish

between heathy and sickle (e.g. disease and trait) clusters. The optimal P_1 - P_2 combination was identified using connectivity and Dunn index. Connectivity indicated how strongly two clusters were connected, while Dunn index indicated intra-cluster compactness and inter-cluster separation [29]. We finally plotted Dunn index vs. connectivity to identify the most robust combination with low connectivity and high Dunn index (right panel) lying in the top right quadrant of the plot.

Figure 5B shows a plot of Dunn index vs. connectivity for 16 $P_1 - P_2$ combinations generated from the roundness distributions of 164 blood samples (H = 49, D = 23 and T = 92) with known hemoglobin profiles. The values of the parameters used in this plot are given in **table S2** in the supporting information. For this experiment, we treated disease samples with 0.1% sodium metabisulphite as the roundness distributions of disease and trait samples are different at this concentration. Similarly, both trait and healthy samples were treated with 0.3% sodium metabisulphite to distinguish them from each other.

There are two points in the top right quadrant corresponding to the roundness ranges of 0.2 – 0.8 (combination #10; $P_1: 0.2 - 0.5$; $P_2: 0.5 - 0.8$) and 0.4 – 1.0 (combination #12, $P_1: 0.4 - 0.7$; $P_2: 0.7 - 1.0$) respectively that meet the selection criteria. Combination 10 (table **S2** in supporting information) includes information about sickle RBCs with 0.2<R<0.4 and excludes information about unsickled RBCs with R>0.8. Combination 12, with the highest Dunn index, lacks information about sickle RBCs with R<0.4, but includes information about unsickled RBCs with R>0.8. As combination 10 contains information about RBCs that are physiologically more relevant to our study, we chose it over combination 12.

Figure 5C shows the P_2 vs. P_1 plot of 164 known samples corresponding to the first combination. We used a support vector machine (SVM) model on this dataset to develop a classifier (shown by the dotted line) that separated healthy and sickle (e.g. disease and trait) blood. A point that lies in the grey parameter space below the classifier should correspond to a blood sample with unsickled RBCs, while a point that lies in the white parameter space above the classifier should correspond to a blood sample with sickled RBCs.

Distinguishing between disease and trait blood using our classifier

Finally, we validated the classifier with 35 unknown blood samples. **Figure 6(A)** shows the work flow, where we treat each unknown sample with both 0.1% and 0.3% sodium metabisulphite and plot the corresponding P_1 and P_2 values (**figure 6B**). We decided upon this work flow because it is not possible to unambiguously identify an unknown blood sample as healthy, disease or trait by treating it with just one sodium metabisulphite concentration. As healthy RBCs do not sickle with either concentration, P_1 and P_2 are low, and the corresponding points (hollow and solid black squares) lie in the grey region below the classifier. In contrast, more than 80% RBCs in disease samples sickle when treated with either 0.1% or 0.3% sodium metabisulphite, resulting in high P_1 and P_2 values. Hence, both points (hollow and solid red circles) corresponding to disease samples lie in the white region above the classifier. As very few RBCs in trait samples sickle when treated with 0.1% sodium metabisulphite, the corresponding point (solid blue triangle) lies below the

classifier. The same trait sample has high P_1 and P_2 values when treated with 0.3% sodium metabisulphite. Therefore, the corresponding point (hollow blue triangle) lies above the classifier.

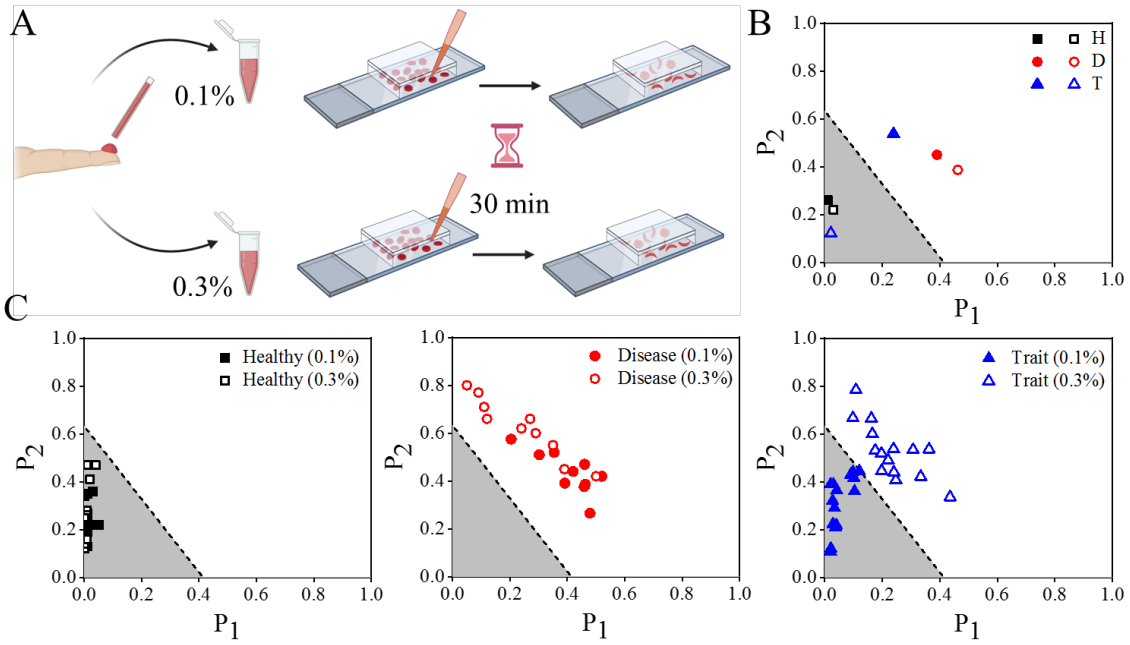

Figure 6. A classification scheme to unambiguously distinguish between disease, trait and healthy blood samples. (A) Workflow to classify an unknown sample. Each unknown sample is treated with two different sodium metabisulphite concentrations (0.1% and 0.3%) and imaged after 30 min. (B) P_2 vs. P_1 plots for healthy, disease and trait samples. Solid and hollow symbols correspond to 0.1% and 0.3% sodium metabisulphite respectively. For a healthy sample both points lie below the classifier (grey region). For a disease sample, both points lie above the classifier (white region). For a trait sample, the point corresponding to 0.1% sodium metabisulphite lies below the classifier, while the point corresponding to 0.3% sodium metabisulphite lies above the classifier. (C) Our technique accurately classified 35 distinct unknown samples (H = 10; D = 10 and T = 15) as shown in the three plots.

We applied the classification scheme to a pilot study and accurately identified thirty-five unknown blood samples (H = 10, D = 10 and T = 15) from adults and older children, as shown in **figure 6C**. We also compared the performance of this classifier with the second classifier (combination 12) identified from the connectivity-Dunn index plot. As shown in **Figure S9** in the supporting information, this classifier too could accurately identify all 35 unknown samples. This is the first proof of concept demonstrating RBC shape as the sole biophysical parameter to distinguish between sickle homozygous (disease) and heterozygous (trait) blood samples with high accuracy. However, this technique is yet to be validated with other hemoglobin variants or blood samples obtained from newborns with high levels of fetal hemoglobin.

Outlook

It is known that hemoglobin polymerization inside a sickle RBC depends on a number of factors, such as, the intracellular HbS concentration, whether HbS exists as homodimer or heterodimer, the presence of other types of hemoglobin (e.g. HbA, HbF, etc.), and the rate of deoxygenation. Hemoglobin polymerization determines the shapes of sickle RBCs under hypoxia. We postulated that RBC populations in trait and disease samples have characteristic shape distributions under different hypoxic conditions, which can be used to distinguish between these two sample types.

We devised a way to induce controlled hypoxia in blood samples by treating them with two different concentrations of a chemical oxygen scavenger (sodium metabisulphite) in a specially designed microfluidic chamber. RBCs of an unknown blood sample, when treated with high and low concentrations of sodium metabisulphite for 30 min, led to characteristic shape profiles. By comparing the profiles of 164 known blood samples, we developed a robust shape-based classifier and used it to accurately identify 35 unknown blood samples in a proof-of-concept study. The use of a portable mobile phone microscope and a disposable microfluidic chip makes this method suitable for confirmed diagnosis of sickle cell disease at the point of care.

Methods

Blood samples. All studies using human blood samples were approved by the Institute Ethics Committee (IEC), IIT Bombay, with approval numbers IITB-IEC/2016/016, IITB-IEC/2017/020 and IITB-IEC/2018/042. Written informed consent to use leftover blood samples was taken from all participants. Leftover de-identified blood samples were collected from adults and older children with a mix of genders during sickle cell screening camps organized by Shirin and Jamshed Guzder Regional Blood Centre (Valsad, Gujarat) and Dayanand Hospital (Talasari, Maharashtra). The ages of the participants ranged from 10 to 60 years. We excluded individuals who (i) were under treatment with folic acid or hydroxyurea, or (ii) received blood transfusion within three months prior to blood collection. Blood samples from self-reported healthy volunteers from IIT Bombay and Dayanand Hospital were used as healthy samples during development and validation of the classifier. All known sickle blood samples (D = 23 and T = 92) were first screened by the hospital personnel using a standard solubility test. Their hemoglobin profiles were then confirmed using HPLC to conclusively identify them as disease or trait.

Experiment protocol. Leftover blood samples were transferred on ice to K3/EDTA-coated vacutainer tubes, brought to IIT Bombay and stored at 4°C. All tests were performed within 48 h of blood collection to minimize crenation of the RBCs due to storage. Sodium metabisulphite solutions were freshly prepared before each experiment due to its shelf life of 3 h. A drop of blood was added to the sodium metabisulphite solution prepared in cell culture media (RPMI-1640). We diluted all blood samples by 20X, irrespective of their hematocrit values. The average pH of blood samples diluted by 20X in 0.1% and 0.3% sodium metabisulphite solution was 6.05 ± 0.2 and 5.83 ± 0.1 respectively. A 10 µl volume of 20X diluted blood mixed with an appropriate concentration sodium metabisulphite was introduced into the imaging chamber and the chip was sealed with

quick-drying transparent nail lacquer. The chip was then placed on the sample stage of the smartphone microscope. Images of RBCs were captured at 0 min and 30 min. We also captured real-time videos of sickling at 30 fps to understand the sickling kinetics. While the ambient temperature of the lab during imaging ranged from 29ºC to 31ºC, the temperature during field testing was found to vary between 25°C and 32°C. High performance liquid chromatography (HPLC) was performed at Shirin and Jamshed Guzder Regional Blood Centre on all blood samples to obtain their hemoglobin profiles (HbA, HBA_2, HbS and HbF).

Image analysis and classification. Brightfield images of unstained RBCs were analyzed by ImageJ following a process flow shown in **figure S10** in the supporting information [30]. We measured roundness and solidity of each RBC and removed those with solidity <0.8 as these corresponded to partially focused RBCs. Roundness values of remaining ~ 150 - 200 RBCs in the field of view were binned into 10 groups with 0.1 width to obtain the roundness distribution. Each distribution was normalized by dividing by the total number of RBCs included in the analysis. We used R programming language [31] to calculate connectivity and Dunn index for all 16 P_1 and P_2 combinations. The connectivity was calculated with 10 nearest neighbors. By applying a support vector machine (SVM) model with a linear kernel and a cost of 10 on the raw data, we obtained a classifier given by the equation: $y = -1.527x + 0.633$.

References:

[1] G. A. Barabino, M. O. Platt and D. K. Kaul, "Sickle Cell Biomechanics," *Annual Review of Biomedical Engineering,* vol. 12, pp. 345-367, 15 August 2010.

[2] W. E. Russell, "Is sickle cell anemia a neglected tropical disease?," *PLoS Negl Trop Dis,* vol. 7, no. 5, p. e2120, 2013.

[3] M. T. Patrick, "Time to invest in sickle cell anemia as a global health priority," *Pediatrics,* vol. 137, no. 6, 2016.

[4] Y. Alapan, A. Fraiwan, E. Kucukal, M. N. Hasan, R. Ung, M. Kim, I. Odame, J. A. Little and U. A. Gurkan, "Emerging point-of-care technologies for sickle cell disease screening and monitoring," *Expert review of medical devices,* vol. 13, no. 12, pp. 1073--1093, 2016.

[5] T. N. Williams, "An accurate and affordable test for the rapid diagnosis of sickle cell disease could revolutionize the outlook for affected children born in resource-limited settings," *BMC medicine,* vol. 13, no. 1, p. 238, 2015.

[6] I. J. Sherman, "The sickling phenomenon, with special reference to the differentiation of sickle cell anemia from the sickle cell trait," *Bull. Johns Hopkins Hosp,* vol. 67, no. 309, p. 19, 1940.

[7] G. A. Daland and W. B. Castle, "A simple and rapid method for demonstrating sickling of the red blood cells: the use of reducing agents," *The Journal of laboratory and clinical medicine,* vol. 3, no. 9, pp. 1082--1088, 1948.

[8] H. A. Itano and L. Pauling, "A rapid diagnostic test for sickle cell anemia," *Blood,* vol. 4, no. 1, pp. 66-68, 1949.

[9] L. Pauling, H. A. Itano, S. J. Singer and I. C. Wells, "Sickle cell anemia, a molecular disease," *Science,* vol. 110, no. 2865, pp. 543-548, 1949.

[10] K. Horiuchi, S. K. Ballas and T. Asakura, "The effect of deoxygenation rate on the formation of irreversibly sickled cells," *Blood,* vol. 71, no. 1, pp. 46-51, 1988.

[11] K. Horiuchi, J. Ohata, Y. Hirano and T. Asakura, "Morphologic studies of sickle erythrocytes by image analysis," *The Journal of Laboratory and Clinical Medicine,* vol. 115, no. 5, pp. 613-620, 01 May 1990.

[12] L. L. Wheeless, R. D. Robinson, O. P. Lapets, C. Cox, A. Rubio, M. Weintraub and L. J. Benjamin, "Classification of red blood cells as normal, sickle, or other abnormal, using a single image analysis feature," *Cytometry: The Journal of the International Society for Analytical Cytology,* vol. 17, no. 2, pp. 159-166, 1994.

[13] T. Asakura, K. Asakura, K. Obata, J. Mattiello and S. K. Ballas, "Blood samples collected under venous oxygen pressure from patients with sickle cell disease contain a significant number of a new type of reversibly sickled cells: Constancy of the percentage of sickled cells in individual patients during steady state," *American journal of hematology,* vol. 80, no. 4, pp. 249-256, 2005.

[14] D. K. Das, C. Chakraborty, B. Mitra, A. K. Maiti and A. K. Ray, "Quantitative microscopy approach for shape-based erythrocytes characterization in anaemia," *Journal of microscopy,* vol. 249, no. 2, pp. 136-149, 2013.

[15] J. Jung, L. E. Matemba, K. Lee, P. E. Kazyoba, J. Yoon, J. J. Massaga, K. Kim, D.-J. Kim and Y. Park, "Optical characterization of red blood cells from individuals with sickle cell trait and disease in Tanzania using quantitative phase imaging," *Scientific reports,* vol. 6, no. 31698, pp. 1-9, 2016.

[16] X. Gual-Arnau, S. Herold-García and A. Simó, "Erythrocyte shape classification using integral-geometry-based methods," *Medical & biological engineering & computing,* vol. 53, no. 7, pp. 623-633, 2015.

[17] W. Delgado-Font, M. Escobedo-Nicot, M. González-Hidalgo, S. Herold-Garcia and A. Jaume-i-Capó, "Diagnosis support of sickle cell anemia by classifying red blood cell shape in peripheral blood images," *Medical & biological engineering & computing,* vol. 58, no. 6, pp. 1265-1284, 2020.

[18] N. Praljak, S. Iram, U. Goreke, G. Singh, A. Hill, U. A. Gurkan and M. Hinczewski, "Integrating deep learning with microfluidics for biophysical classification of sickle red blood cells," *bioRxiv,* 2020.

[19] B. Javidi, A. Markman, S. Rawat, T. O'Connor, A. Anand and B. Andemariam, "Sickle cell disease diagnosis based on spatio-temporal cell dynamics analysis using 3D printed shearing digital holographic microscopy," *Optics Express,* vol. 26, no. 10, pp. 13614-13627 , 2018.

[20] K. de Haan, H. C. Koydemir, Y. Rivenson, D. Tseng, E. Van Dyne, L. Bakic, D. Karinca, K. Liang, M. Ilango, E. Gumustekin and A. Ozcan, "Automated screening of sickle cells using a smartphone-based microscope and deep learning," *NPJ Digital Medicine,* vol. 3, no. 1, pp. 1-9, 2020.

[21] W. A. Eaton and J. Hofrichter, "Hemoglobin S gelation and sickle cell disease," *Blood,* vol. 70, no. 5, pp. 1245-1266, 1987.

[22] W. E. Mickols, J. D. Corbett, M. F. Maestre, I. Tinoco, J. Kropp and S. H. Embury, "The effect of speed of deoxygenation on the percentage of aligned hemoglobin in sickle cells. Application of differential polarization microscopy," *Journal of Biological Chemistry,* vol. 263, no. 9, pp. 4338-4346, 1988.

[23] J. D. Corbett, W. E. Mickols and M. F. Maestre, "Effect of hemoglobin concentration on nucleation and polymer formation in sickle red blood cells," *Journal of biological chemistry,* vol. 270, no. 6, pp. 2708-2715, 1995.

[24] K. D. Pagana and T. J. Pagana, Mosby's Manual of Diagnostic and Laboratory Tests-E-Book, Elsevier Health Sciences, 2017.

[25] F. A. Ferrone, J. Hofrichter and W. A. Eaton, "Kinetics of sickle hemoglobin polymerization: II. A double nucleation mechanism," *Journal of molecular biology,* vol. 183, no. 4, pp. 611-631, 1985.

[26] W. A. Eaton and J. Hofrichter, "Sickle cell hemoglobin polymerization," in *Advances in protein chemistry*, vol. 40, C. B. Anfinsen, J. T. Edsall, F. M. Richards and D. S. Eisenberg, Eds., Elsevier, 1990, pp. 63-279.

[27] M. Rotter, D. Yosmanovich, R. W. Briehl, S. Kwong and F. A. Ferrone, "Nucleation of sickle hemoglobin mixed with hemoglobin A: experimental and theoretical studies of hybrid-forming mixtures," *Biophysical Journal,* vol. 101, no. 11, pp. 2790-2797, 2011.

[28] J. M. Higgins, D. T. Eddington, S. N. Bhatia and L. Mahadevan, "Sickle cell vasoocclusion and rescue in a microfluidic device," *Proceedings of the National Academy of Sciences,* vol. 104, no. 51, pp. 20496-20500, 2007.

[29] J. Handl, J. Knowles and D. B. Kell, "Computational cluster validation in post-genomic data analysis," *Bioinformatics,* vol. 21, no. 15, pp. 3201-3212, 2005.

[30] C. A. Schneider, W. S. Rasband and K. W. Eliceiri, "NIH Image to ImageJ: 25 years of image analysis," *Nature methods,* vol. 9, no. 7, pp. 671-675, 2012.

[31] R Core Team, "R: A language and environment for statistical computing," R Foundation for Statistical Computing, Vienna, Austria, 2013.

[32] J. V. Neel, "The inheritance of sickle cell anemia," *Science,* vol. 110, no. 2846, pp. 64-66, 1949.

[33] X. Lu, A. Chaudhury, J. M. Higgins and D. K. Wood, "Oxygen-dependent flow of sickle trait blood as an in vitro therapeutic benchmark for sickle cell disease treatments," *American journal of hematology,* vol. 93, no. 10, pp. 1227-1235, 2018.

[34] X. Lu, D. K. Wood and J. M. Higgins, "Deoxygenation reduces sickle cell blood flow at arterial oxygen tension," *Biophysical journal,* vol. 110, no. 12, pp. 2751-2758, 2016.

[35] J. C. Dunn, "Well-separated clusters and optimal fuzzy partitions," *Journal of cybernetics,* vol. 4, no. 1, pp. 95-104, 1974.

411

412

Acknowledgements

The authors would like to thank Dr. Yazdi Italia, Sister Lavina, Sister Molly, Sister Monica, Mr. Bhavesh Raicha, Mr. Manoj Parekh, the staff at Shirin and Jamshed Guzder Regional Blood Centre (Valsad), and the staff at Dayanand Hospital (Talasari) for use of leftover blood samples and sharing of de-identified HPLC results. They acknowledge Dr. G. Nageshwara Rao, Dr. Kanjaksha Ghosh, Dr. Roshan Colah, Dr. Malay Mukherjee and Dr. Manisha Madkaikar for technical discussions, Dr. Santosh Noronha for use of dissolved oxygen meter, and Mr. Devendra Dhaka, Mr. Binil Jacob, Mr. Siddhant Jaitpal and Mr. Santosh Jinnawar for other technical and logistical support to the project. This project was supported by a Grand Challenges Explorations (phase 1) grant from Bill and Melinda Gates Foundation through their IKP-GCE program and a translation grant from Tata Centre for Technology and Design (TCTD), Indian Institute of Technology Bombay. R.M. and A.M. received salary support from a grant funded by the Wadhwani Research Centre for Bioengineering (WRCB), Indian Institute of Technology Bombay. The authors are grateful to Dr. Shamik Sen, Dr. Anirban Sain and Dr. Suchita Nath-Sain for their critical feedback on the manuscript. Parts of figures 1, 2 and 6 were created with BioRender.com.

Author contributions

C.D., O.S., R.M., M.S., S., P.G. and D.P. designed research. C.D., O.S., R.M., M.S., S., S.S., A.M., P.G., N.M., and S.S. performed research. C.D., O.S., R.M., S.S., A.M., P.G., S.S. and D.P. analyzed data. R.M., C.D., O.S., P.G. and D.P. wrote the paper.

Supporting information

1. Optimizing the microfluidic chip height

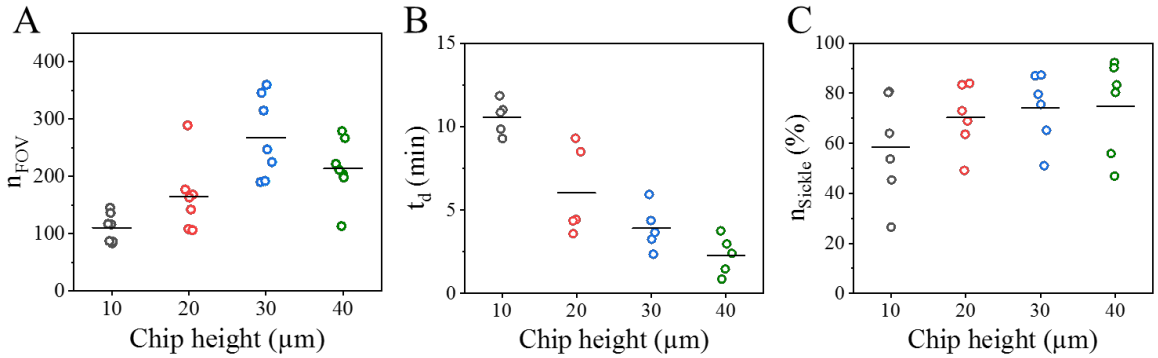

Figure S1: Optimization of the height of the microfluidic chamber. (A) Number of healthy RBCs in the field of view (n_{FOV}) inside imaging chambers of different heights. The line indicates the mean value (n =7). (B) The time taken (t_d) for the first RBC in the field of view to start sickling inside chips of different heights (N =6). (C) The percentage of sickle cells (n_{sickle}) at t = 30 min inside chips of different heights (N = 6).

The material of the microfluidic imaging chamber must be impermeable to oxygen and have good optical properties for imaging unstained sickled RBCs. As shown in **figure 1B**, we made 10 mm × 22 mm microfluidic imaging chambers in glass. We used commercial double-coated thin adhesive films of specific thicknesses as spacers to define the chamber height. We explored chamber heights of 10 µm, 20 µm, 30 µm, 40 µm, 80 µm and 100 µm, and tested these chips by imaging healthy blood samples. Fabricated devices were not used when (i) an irregular diffraction pattern was observed indicating non-uniform thickness, (ii) introducing the sample into the chamber by capillary action was difficult, (iii) air bubbles remained trapped after loading blood and sealing the chip, or (iv) significant crenation occurred in RBCs immediately after loading.

While choosing the most optimal chip height, we need to ensure that (i) we avoid shear stress to RBCs while trying to fill a chamber with a very small height and (ii) that the RBCs have enough room to sickle inside the microfluidic chip. We noticed that an increase in the microfluidic confinement by reducing the chamber height increased crenation of healthy RBCs. While an increased device height reduced crenation and promoted free sickling, it led to stacking of RBCs. Therefore, we performed subsequent experiments with chips of height 10, 20 30 and 40 µm.

Figure S1(left panel) shows the number of RBCs counted in the field of view (n_{FOV}) inside chambers of height 10 µm, 20 µm, 30 µm and 40 µm. Considerably fewer RBCs are counted in

10 µm (110 ± 10; mean ± SEM) and 20 µm (165 ± 23) high chambers. In contrast, the image processing algorithm detects more than 200 RBCs in the field of view inside chambers of 30 µm (268 ± 27) and 40 µm (213 ± 21) heights. The number of RBCs detected inside the chamber increases with an increase in the chamber height. As there are more densely packed RBCs inside a 40 µm high chip, these are eliminated as clusters by the image processing algorithm. This results in a decrease in the number of RBCs counted by the algorithm inside the 40 µm high chip.

As shown in **figure S1 (middle panel)**, we treated six sickle cell disease blood samples with 0.1% sodium metabisulphite. From the real time videos of sickling, we measured the time (t_d) it takes for the first RBC to sickle inside imaging chambers of different heights. The values of t_d are 10.6 ± 0.5 min (mean ± SEM), 6.0 ± 1.2 min, 3.9 ± 0.6 min and 2.3 ± 0.5 min for chip heights of 10, 20, 30 and 40 µm respectively. We also measured the percentage of sickled RBCs (n_{sickle}) at $t = 30$ min inside chips of different heights. As shown in **figure S1 (right panel)**, the mean value of n_{sickle} ranged from 58% to 75% with a large variability in the data.

We found that RBCs inside a 30 µm high chip do not crenate much and sickle relatively fast (t_d = 3.9 ± 0.6 min). On an average, there are > 250 RBCs in the field of view in the 30 µm high chip. Therefore, all further experiments in this study were conducted inside 30 µm high chips.

2. Design and development of an inverted portable smartphone microscope

We designed and developed a single-objective inverted transmission microscope to capture images of unstained RBCs suspended in liquid media and record their sickling kinetics in real time at low-resource settings. **Figure S2(A)** shows a photo of the smartphone microscope. The user can rotate the phone holder by any angle from 0º to 90º for comfortable viewing, while keeping the image in focus. We designed and 3D-printed two kinds of holders to accommodate Xiaomi Mi3 and Samsung A10 phone models. The smartphone can be easily detached from the holder by the user when the microscope is not being used.

Figure S2(B) shows the exploded view of the mechanical assembly. A microscope slide or a microfluidic chip is placed on the sample stage. The sample stage is attached to a second stage (called “Z-movement stage” in our diagram) capable of vertical movement.

This arrangement allows us to move the sample stage up or down by turning the focusing knob. Therefore, the sample stage, and not the objective, is moved while focusing the image in our design. The focusing knob has a pitch of 0.25 mm. The Z-movement stage is fixed to the base plate of the microscope. The entire focusing arrangement and the base plate are made of aluminium to make the microscope stable. The base plate also supports another metallic vertical arm containing the objective lens holder. A key feature of the mechanical system of our microscope is the presence of a 3D-printed rotating arm containing the optical components and the smartphone holder. This arm can be rotated by any angle from 0º to 90º to change the viewing angle of the smartphone. The outer casing of the microscope is 3D-printed in PLA.

Figure S2(C) shows the optical components, while **figure S2(D)** shows the light path. A 1W white LED, fitted with a collimating lens, acts as the illumination source. The light transmitted from the microfluidic chip passes through a 40X (0.65 NA) air objective and falls on a right-angled prism (prism #1 in the figure), which bends the beam by 90°. Another right-angled prism (prism #2 in the figure) bends the beam by another 90° such that it falls on an eye-piece lens with 15X magnification. A total magnification of 600X (using a 40X objective and a 15X eye-piece) is achieved in our microscope over a tube length of 160 mm.

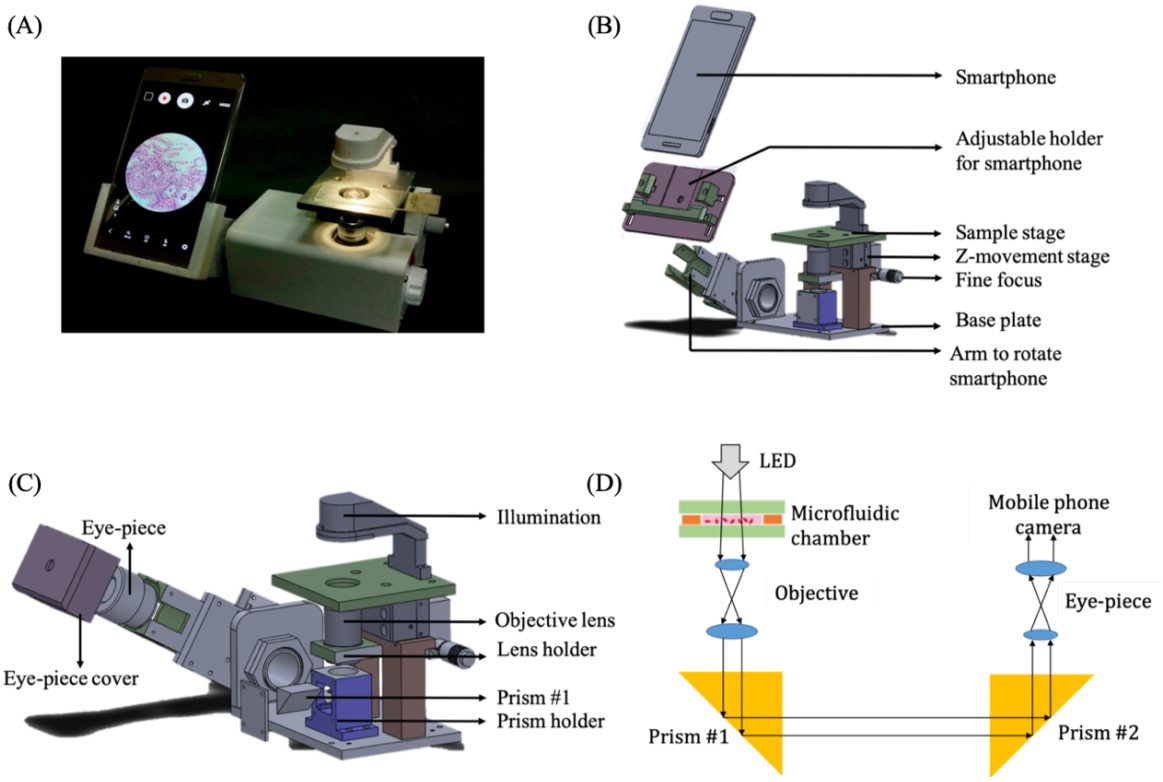

Figure S2. An inverted single-objective portable smartphone microscope. (A) A photo of the microscope is shown. (B) Exploded 3D schematic of the mechanical parts of the microscope showing the sample and the Z-movement stages, the phone holder, the focusing knob, and the rotating arm. (C) Exploded 3D schematic of the optical system of the microscope showing the light source and various lenses and prisms. (D) Ray diagram showing the light path inside the microscope.

The system of two prisms makes the microscope design compact. The rotating arm contains the second prism, the eye-piece and the mobile phone holder. The rotating arm is mounted in such a way that (i) the incident surface of the second prism always remains parallel to the emitting surface of the first prism during rotation, and (ii) the emitting surface of the second prism remains parallel to the eye-piece. The arm rotates in a plane orthogonal to the beam connecting the two prisms. The

3D-printed smartphone holder is detachable and we customized it to the specific mobile phone models. We used a 3D printed PLA cover for the eye-piece to have a fixed distance between the eye-piece and the smartphone camera such that a sharp and focused image forms on the phone screen. The smartphone holder slides onto a slot on the eye-piece cover and keeps the camera in perfect alignment with the rest of the optical system.

3. Deoxygenation rate depends on oxygen scavenger concentration

We plotted the dissolved oxygen concentration as a function of time for different sodium metabisulphite concentrations (**figure 3A** in the manuscript). We fitted each plot to an equation of the functional form $y = Ae^{-\frac{x}{\tau}} + \mathrm{B}$, where y indicates the dissolved oxygen content (%) and x indicates time (min). **Table S1** shows the fitting parameters for each concentration.

Table S1: Fitting parameters to extract the decay time constant (τ) describing the decrease in dissolved oxygen present in RPMI-1640 for different concentrations of the oxygen scavenger sodium metabisulphite.

Sodium metabisulphite	0.1%	0.2%	0.3%	0.4%	0.5%
A	112.5	117.1	106.6	100.7	99.6
B	- 7.2	- 4.5	- 0.9	0.2	0.8
τ (min)	12.2	9.3	6.1	3.5	1.6

4. Choice of diluent and dilution factor

The buffer used to dilute blood must keep RBCs under minimal osmotic stress to avoid crenation, while the dilution factor should ensure that there is an adequate number of RBCs in the field of view. We first diluted healthy RBCs using 0.9% normal saline (NS), 5% dextrose, 1X phosphate buffered saline (PBS) and cell culture media (RPMI-1640). 5% dextrose led to clumping of healthy RBCs and was discarded. Next, sodium metabisulfite solutions of appropriate concentrations as discussed in the manuscript were prepared in NS, PBS and RPMI-1640 and were added to whole blood from trait and disease patients. Compared to RPMI-1640, sickling in PBS and normal saline took 2-3 times longer. Therefore, we continued our study with RPMI-1640 as the diluent.

The dilution was adjusted in such a way that the cells do not form stacks in the imaging chamber. As seen in **figure S3**, whole blood showed strong rouleaux formation. There were too many RBCs present in the field of view with 5X diluted blood, making it difficult for the image processing program to identify individual RBCs. The cells were sparsely distributed for 20X and 40X

547 dilutions. However, there were too few cells in the field of view when blood was diluted by 40X,
548 60X or 100X. Dilutions higher than 40X also showed an increase in crenation. Therefore, we
549 decided to continue our experiments with 20X dilution.

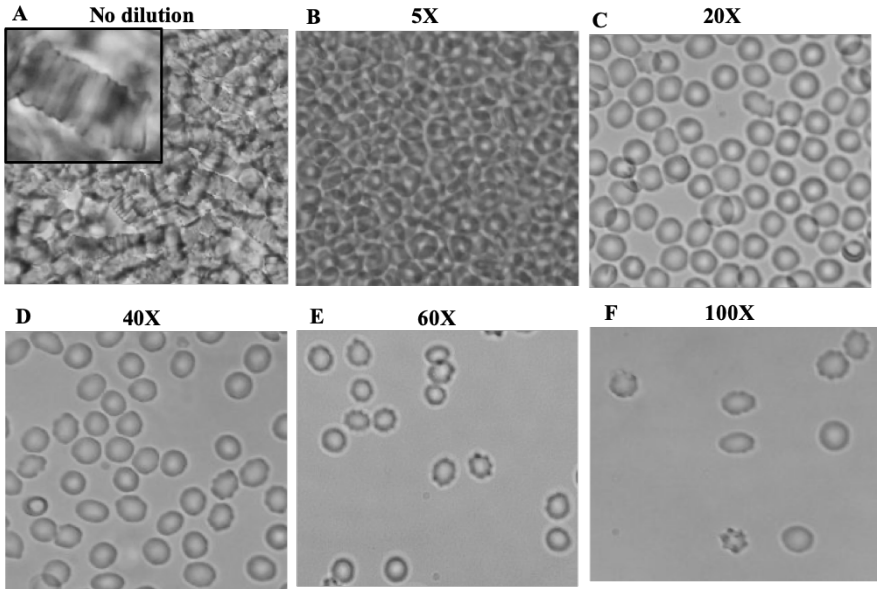

550

551 *Figure S3. Images of RBCs with different dilutions. (A) Strong rouleaux formation is seen with*
552 *undiluted blood. (B) There are too many RBCs at 5X dilution, making it difficult for an image*
553 *processing program to distinguish individual cells. (C) A dilution of 20X gives a sufficient number*
554 *of cells in the field of view. (D – F) Dilutions of 40X, 60X and 100X lead to very few cells in the*
555 *field of view, making it difficult to obtain reliable statistical data.*

556

557

558

559 **5. Raw images of disease, trait and healthy samples treated with sodium metabisulphite for**
560 **30 min**

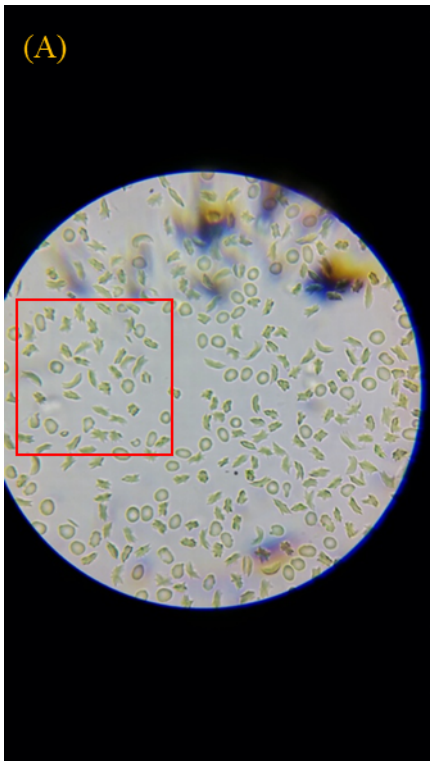

Filename: D126_0.1_30min_20170106_212209

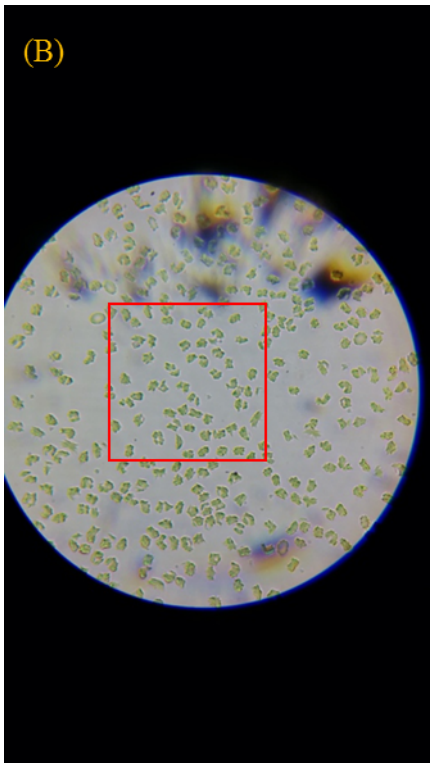

Filename: D126_0.3_30min_20170106_221552

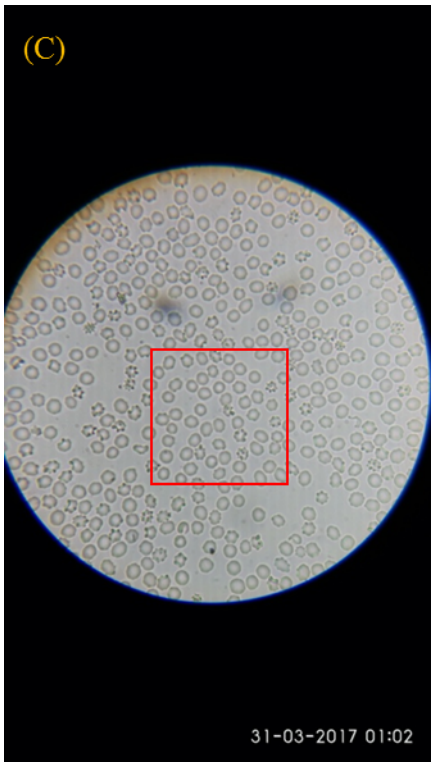

Filename: T163_0.1_30min_20170331_010215

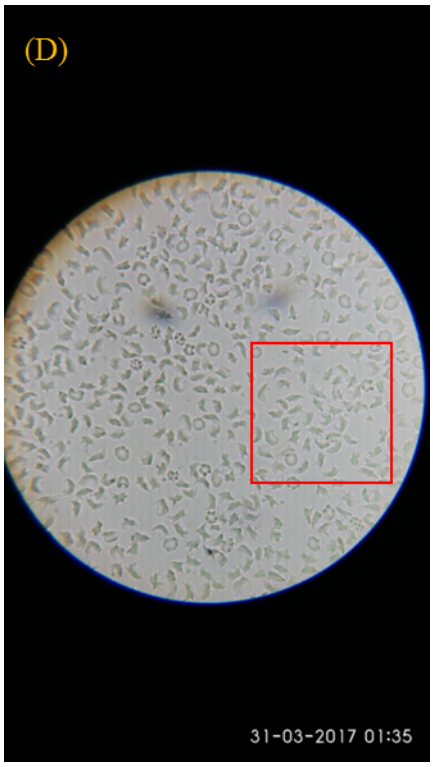

Filename: T163_0.3_30min_20170331_013525

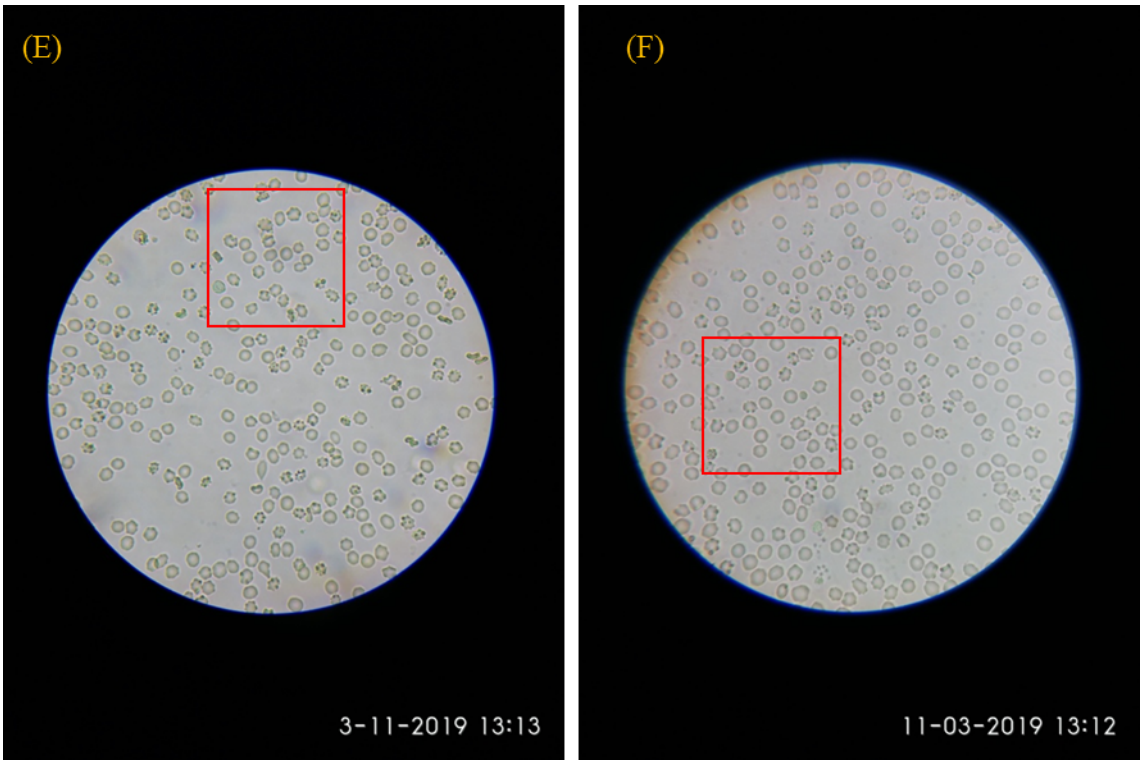

Filename: N07_0.1_30min _20190311_131331 Filename: N07_0.3_30min_20190311_131210

Figure S4. Raw images of disease (A and B), trait (C and D) and healthy (E and F) samples treated with 0.1% (left column) and 0.3% (right column) sodium metabisulphite respectively. The red rectangles show the areas from which snippets were taken for figure 4A.

Figure S4 shows some representative raw images of disease, trait and healthy blood samples. The red rectangles show the areas that were used as snippets in figure 4 of the manuscript.

6. Choosing roundness (R) over form factor (FF) to characterize RBC shapes

We explored both roundness and form factor for characterising individual RBC shapes in our study. We imaged healthy blood samples and measured both these parameters using ImageJ for RBCs that are very close to circular in shape. Note that the parameter 'form factor (FF) reported by Wheeless and others [12] is the same as the parameter 'circularity' (C) measured by ImageJ. As shown by equations (1) and (2), both R and FF range from 0 for elongated objects to 1 for perfect circles.

$$FF = \frac{4\times\pi\times Area}{Perimeter^2} \qquad (1)$$

$$R = \frac{4\times Area}{\pi\times Major\ axix^2} \qquad (2)$$

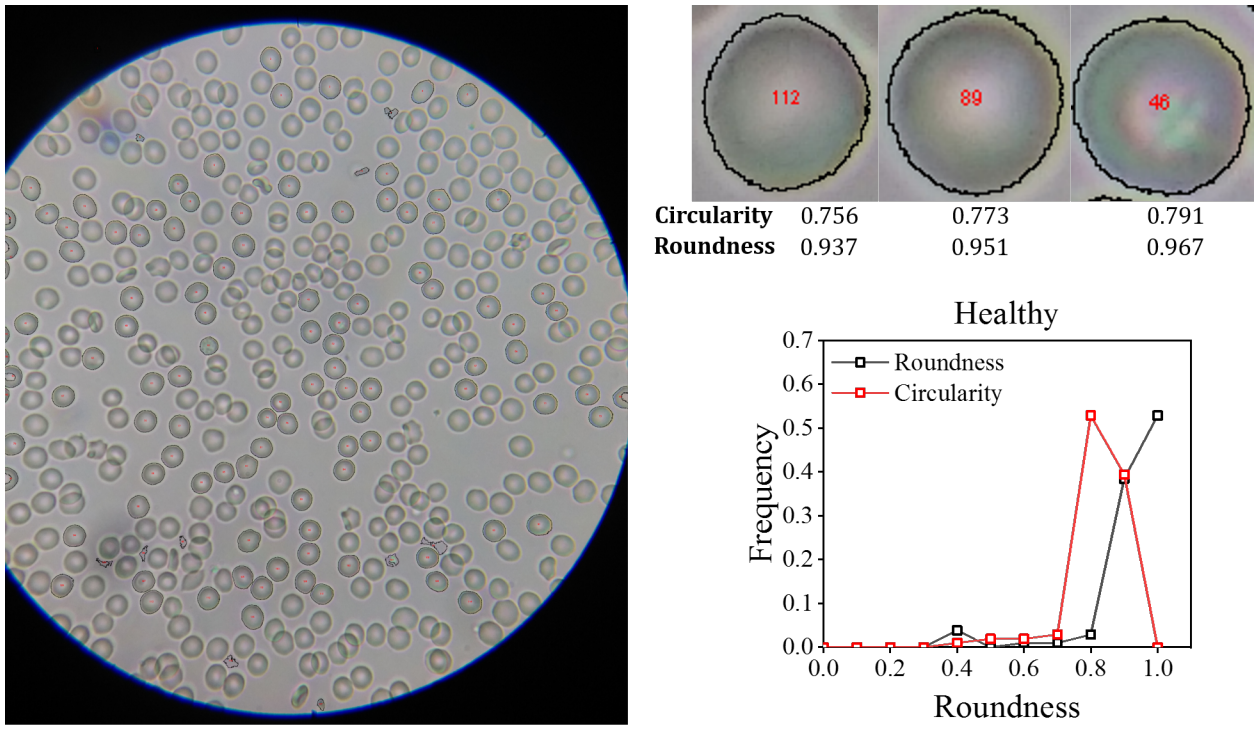

Figure S5: Comparing roundness and form factor for characterizing individual RBC shapes. An image of a healthy flood sample is shown. The circularity and roundness values of three apparently circular RBCs in this image are also shown. As expected, the roundness distribution of the healthy sample peaks at 0.9-1.0, while the form factor (measured as circularity by ImageJ) peaks at 0.8.

Figure S5 shows the image of a healthy blood sample. Three individual RBCs (numbered 112, 89 and 46) that appear circular in this image are shown separately with their corresponding shape parameters. While the roundness values of these RBCs are >0.9, the form factor is ~ 0.7. This is because the form factor formula uses the value of the measured perimeter, which is more sensitive to the pixels in the boundary of an object. Therefore, the use of form factor in our image analysis could introduce artifacts in the brightfield images of sickle cells that often have blurred boundaries. On the other hand, the formula for roundness uses the value of the major axis, which is not sensitive to the pixels at the boundary of an object. Therefore, we used roundness to describe the shapes of irregular objects such as sickle RBCs.

7. RBC shapes in disease samples treated with 0.1% sodium metabisulphite

When we treat a disease sample with 0.1% sodium metabisulphite, we see holly leaf and granular RBCs in addition to sickle RBCs, as discussed in the manuscript. An image of a representative disease sample is manually annotated by an experienced user. We find that out of 282 RBCs in the field of view, there are 100 (35%) sickle, 76 (27%) holly leaf and 63 (22%) granular RBCs). There are also 33 unsickled (12%) RBCs and 10 (4%) RBCs that could not be categorized.

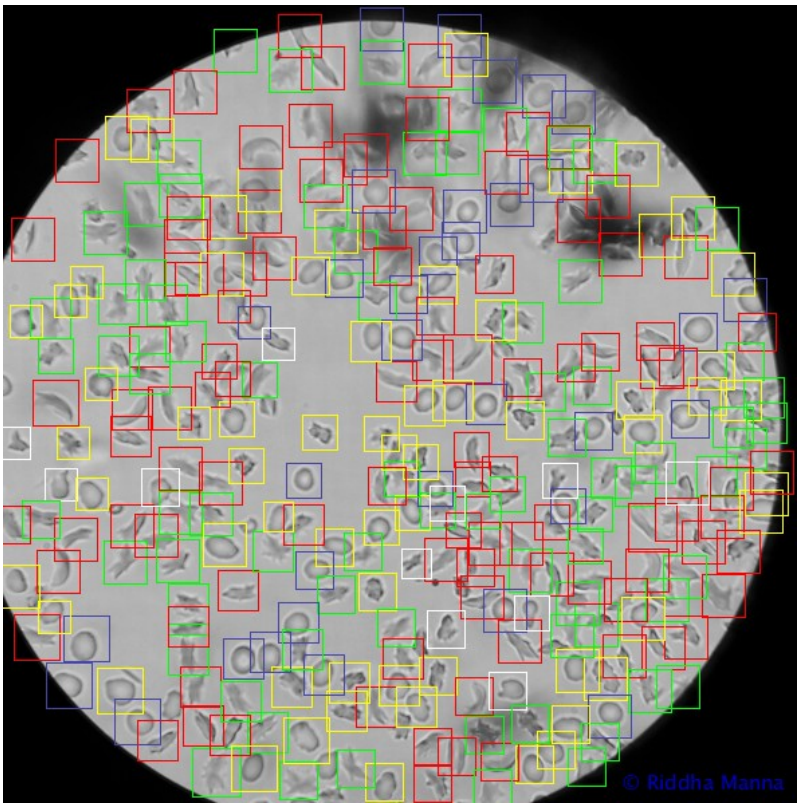

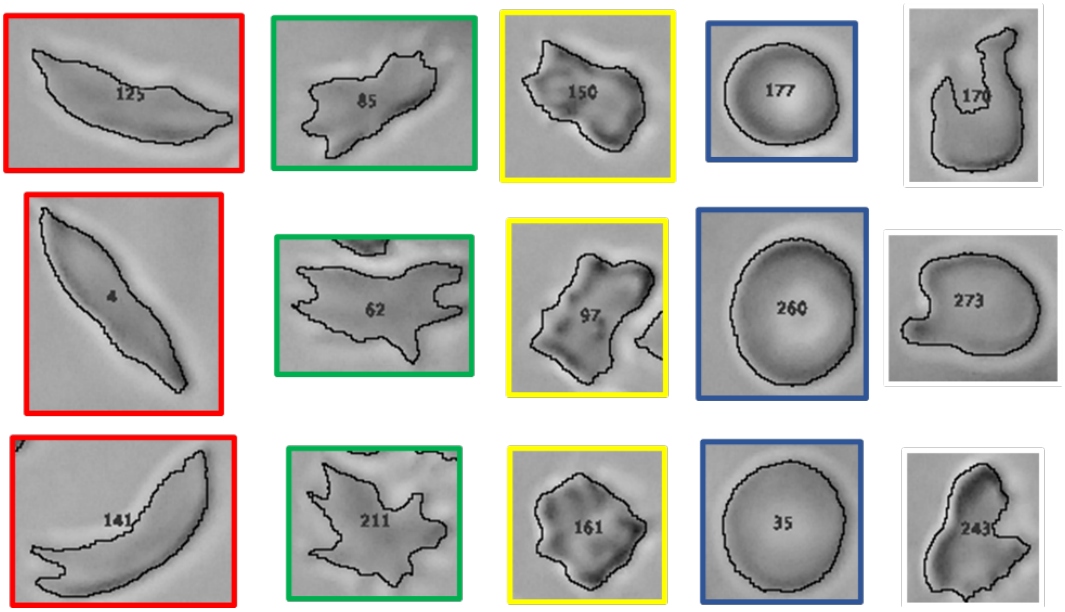

Figure S6. Image of the disease sample (D126) shown in figure S4(A) after manual annotation by an experienced user. We see sickle (red rectangles), holly leaf (green rectangles), granular (yellow rectangles), unsickled (blue rectangles) and uncategorized (white rectangles) RBCs. Three examples of each cell type are shown separately below the image.

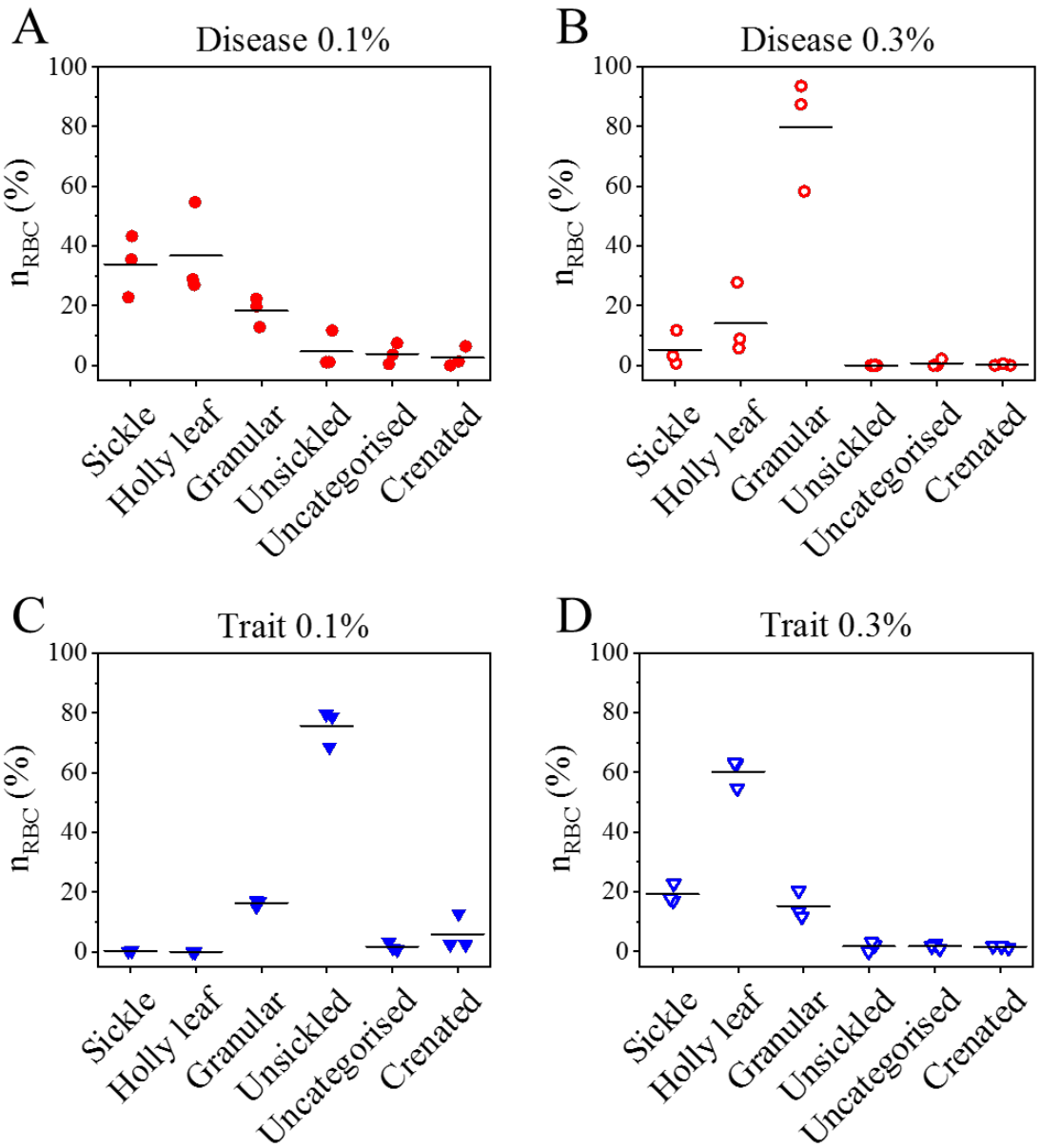

Figure S7. Distribution of RBC shapes in deoxygenated disease (N = 3) and trait (N = 3) samples. (A, B) Disease samples treated with 0.1% and 0.3% sodium metabisulphite. (C, D) Trait samples treated with 0.1% and 0.3% sodium metabisulphite. The horizontal lines indicate the mean values.

We manually annotated and counted the RBCs in three disease and three trait samples, each treated with 0.1% and 0.3% sodium metabisulphite. **Figure S7** shows the number of RBCs of each type in each of these samples. We note that disease samples treated with 0.1% sodium metabisulphite have primarily a mix of sickle (34 ± 6%; mean ± SEM), holly leaf (37 ± 9%) and granular (18 ± 3%) RBCs. The same samples, when treated with 0.3% concentration, have on an average (80 ± 11%) granular and (14 ± 7%) holly leaf RBCs. Trait samples treated with 0.1% metabisulphite

have (76 ± 4%) unsickled RBCs. These samples have (19 ± 2%) sickle, (60 ± 3%) holly leaf and (15 ± 3%) granular RBCs when treated with 0.3% metabisulphite concentration.

8. Image artifacts in healthy blood samples leading to tails in roundness distributions

Figure 4C of the manuscript shows that the roundness distributions of healthy samples have tails at values of R<0.8. As shown in **figure S8**, this is due to the presence of specific artifacts such as RBCs lying sideways (left panel), crenated RBCs (middle panel) or two or more RBCs overlapping in such a way that the area and solidity filters cannot exclude them (right panel). Our area filter, described in section 11 of the supporting information, is chosen to ensure that most sickle cells, which are somewhat larger in area compared to healthy biconcave RBCs, are included in our analysis. This area filter cannot exclude these artifacts when dealing with healthy blood samples. However, the presence of the artifacts do not affect our workflow as seen from the data presented in **figure 5** and **figure 6** of the manuscript.

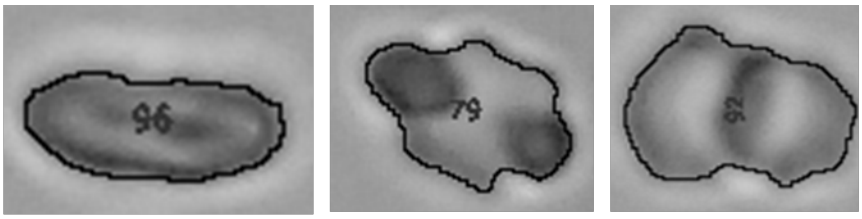

Area:	4620	1774	2767
Roundness:	0.61	0.391	0.62
Solidity:	0.924	0.947	0.899

Figure S8. Images of selected RBCs from a healthy sample (N03) showing RBCs lying sideways (left panel), crenated RBCs (middle panel) or overlapping RBCs (right panel).

9. Details of the P_1 and P_2 combinations used to construct the Dunn index vs. connectivity plot

Table S2: Details of the parameters used to plot Dunn index vs. connectivity

Combination number	***Window size***	***Roundness range for P_1***	**Roundness range for P_2**	**Connectivity**	**Dunn index**
1	0.2	0.0 – 0.2	0.2 – 0.4	2.01	0.07
2	0.2	0.1 – 0.3	0.3 – 0.5	4.97	0.02
3	0.2	0.2 – 0.4	0.4 – 0.6	14.75	0.03
4	0.2	0.3 – 0.5	0.5 – 0.7	4.56	0.07
5	0.2	0.4 – 0.6	0.6 – 0.8	15.07	0.08
6	0.2	0.5 – 0.7	0.7 – 0.9	11.31	0.07
7	0.2	0.6 – 0.8	0.8 – 1.0	4.03	0.06
8	0.3	0.0 – 0.3	0.3 – 0.6	7.07	0.02
9	0.3	0.1 – 0.4	0.4 – 0.7	12.42	0.05
10	**0.3**	**0.2 – 0.5**	**0.5 – 0.8**	**4.16**	**0.08**
11	0.3	0.3 – 0.6	0.6 – 0.9	8.15	0.06
12	**0.3**	**0.4 – 0.7**	**0.7 – 1.0**	**3.45**	**0.14**
13	0.4	0.0 – 0.4	0.4 – 0.8	11.01	0.09
14	0.4	0.1 – 0.5	0.5 – 0.9	11.36	0.02
15	0.4	0.2 – 0.6	0.6 – 1.0	6.77	0.02
16	0.5	0.0 – 0.5	0.5 – 1.0	6.30	0.00

Table S2 lists the parameters used to plot the Dunn index and connectivity values for sixteen different combinations of P_1 and P_2. We varied window widths from 0.2 to 0.5. Combination numbers 10 and 12 with window widths of 0.3 each indicate the most promising combinations and these were used to analyze the data of 35 unknown samples.

10. An alternate classification scheme

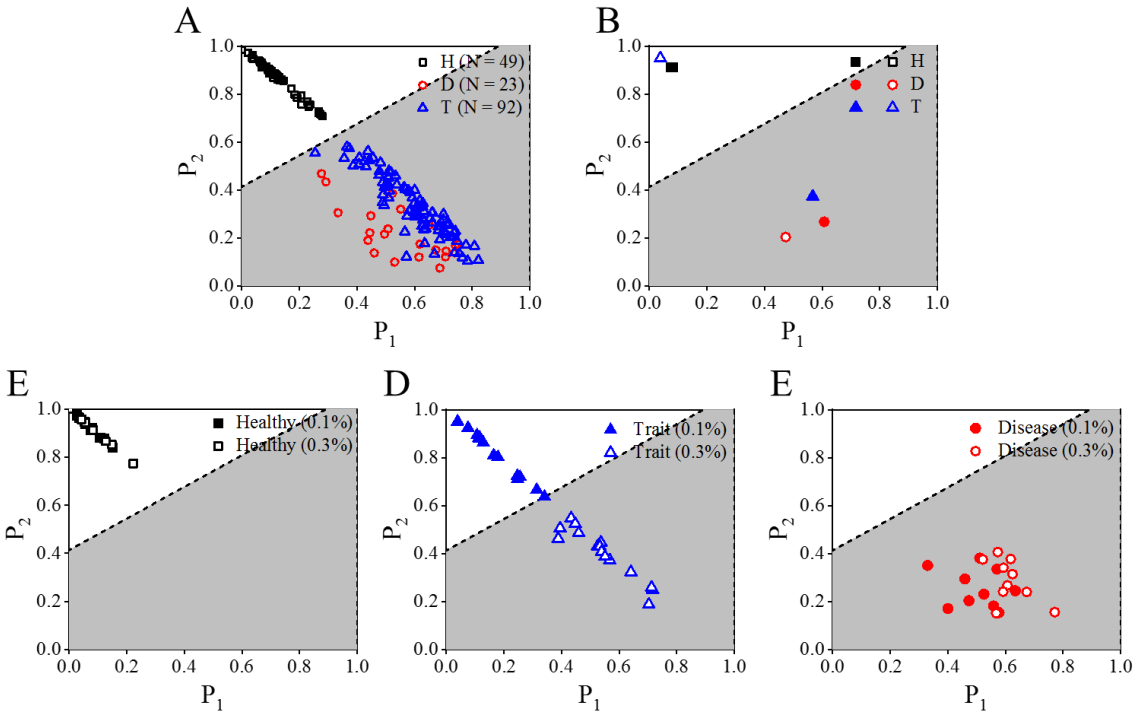

Figure S9. An alternate classifier based on the parameter values of P_1: 0.4 – 0.7 and P_2: 0.7 – 1.0. (A) In a plot of 164 known samples (H = 49, D = 23 and T = 92), the dotted line indicates the classifier that separates healthy and sickle blood samples. The white area in all the plots indicates the parameter space for healthy samples, while the grey area indicates the parameter space for sickle (disease and trait) samples. (B) Both points corresponding to a healthy sample treated with 0.1% and 0.3% sodium metabisulphite lie above the classifier, while the corresponding points for a disease sample lie below the classifier. The point corresponding to a trait sample treated with 0.1% sodium metabisulphite lies in the space (white area) for healthy samples. The point for a trait sample treated with 0.3% sodium metabisulphite lies in the sickle (grey) zone. (C-E) Validation data for healthy (H = 10), trait (T = 15) and disease (D = 10) samples. All 35 unknown samples were accurately identified by this classifier

11. Workflow for image analysis of RBCs

RGB images captured by the smartphone are converted into 8-bit grayscale images. After background subtraction and automatic thresholding, morphological operations are performed to obtain the outlines of the RBCs. Using an area filter, we rule out RBCs with areas <500 pixels (~2.5 μm^2) as possible debris > 7500 pixels (~9.8 μm^2) as clusters of RBCs. The detailed steps in ImageJ are described below.

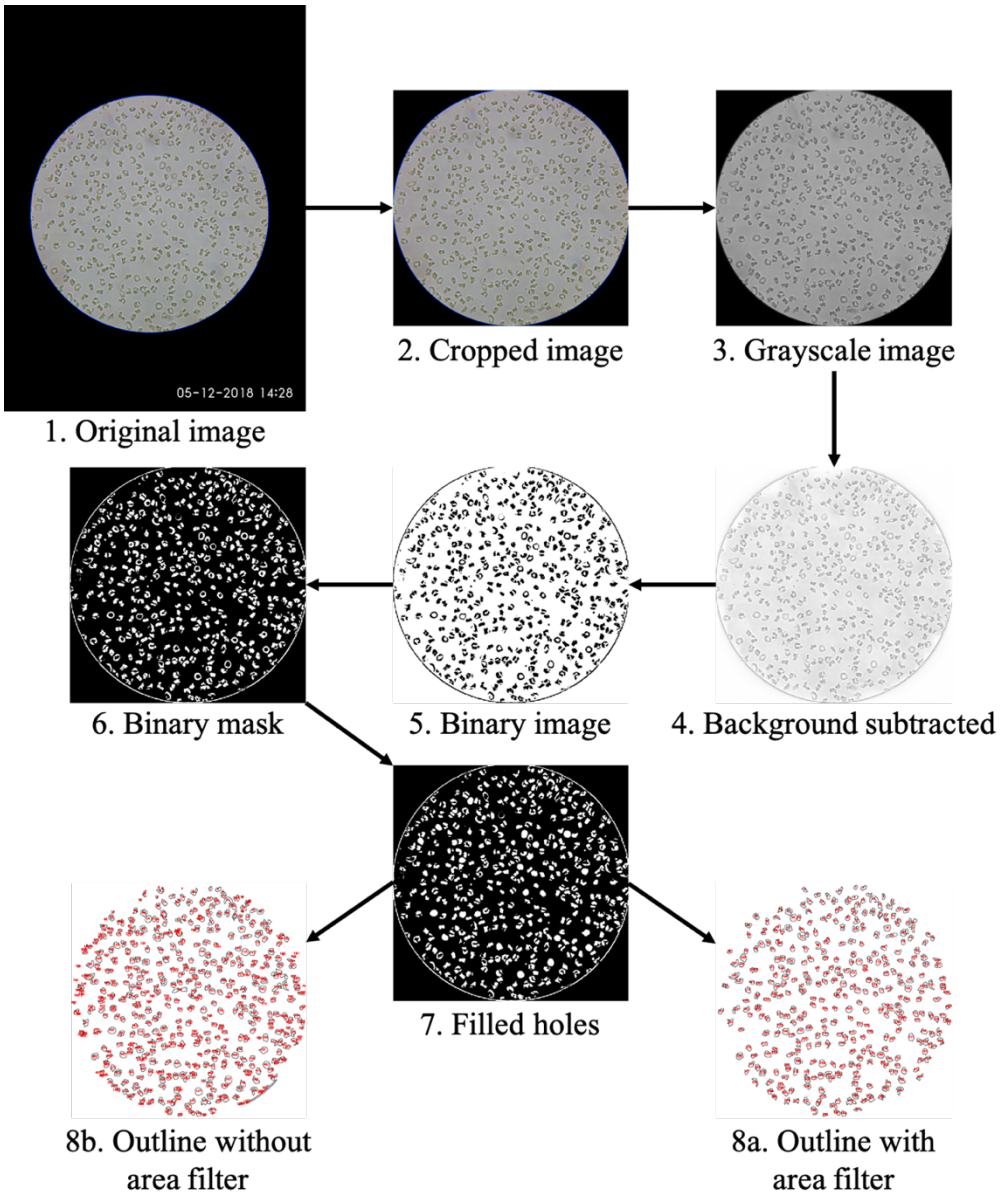

661

662 *Figure S10. The steps involved in image analysis. The original image (1) is opened in ImageJ and*
663 *the area of interest is cropped (2). Then image is converted into an 8-bit grayscale image (3) and*
664 *its background is subtracted to bring the RBCs in the foreground (4). The image is then binarized*
665 *(5) and converted into a binary mask (6) to get the RBCs as white particles. The holes in the*
666 *particles are filled to fill the center of the unfocused part of biconcave RBCs (7). Then the RBCs*
667 *are analyzed to get their solidity, roundness values and outlines. 8a shows the outlines of the RBCs*
668 *when an area filter is applied to fit the RBC sizes, while 8b shows the outlines without an area*
669 *filter.*

670

The captured image **(1)** is first cropped **(2)** to fit the field of view and converted into an 8-bit grayscale image **(3).** We then subtract the background with a rolling ball radius of 50 pixels **(4).** Next, we make the grayscale image into a binary one using the automatic thresholding algorithm of ImageJ. The RBCs appear black on a white background **(5).** This binary image is them converted into a mask, to make the RBCs appear white against a black background **(6)**. On the masked binary image, we perform the operation 'fill holes' **(7)**. This is required as the central part of the biconcave RBCs remain out of focus, making these RBCs appear doughnut-shaped in the binary image. We then analyze the particles (RBCs) to get a list of unique identifiers for each RBC and their shape descriptors including roundness and solidity. Next, we apply an area filter described earlier to exclude debris and connected cells (**8a**). The panel **8b** shows the same cells without the area filter. We then apply a solidity cut-off, where all RBCs with solidity <0.8 are excluded. The RBCs remaining after this step are used to plot the roundness distributions.

12. Captions of movies uploaded as supporting information

Movie 1: Sickling video of a disease sample treated with 0.1% sodium metabisulphite. The 30 min video has been sped up 29.5 times. The sample ID is D188.

Movie 2: Sickling video of a disease sample treated with 0.3% sodium metabisulphite. The 30 min video has been sped up 29.8 times. The sample ID is D188.

Movie 3: Sickling video of a trait sample treated with 0.1% sodium metabisulphite. The 30 min video has been sped up 29.5 times. The sample ID is T187.

Movie 4: Sickling video of a trait sample treated with 0.3% sodium metabisulphite. The 30 min video has been sped up 29.5 times. The sample ID is T187.